

RESEARCH ARTICLE

10.1002/2016JA023773

Key Points:

- The first thermosphere-ionosphere Fe/Fe⁺ (TIFe) model has been developed from first principles for polar regions at the University of Colorado
- TIFe model formulates the TIFe theory depicting the lifecycle of meteoric metals via deposition, transport, chemistry, and wave dynamics
- Antarctic lidar observations were reproduced by TIFe model via neutralization of upward transported and wind shear-converged Fe⁺ layers

Correspondence to:

X. Chu,
xinzhao.chu@colorado.edu

Citation:

Chu, X., and Z. Yu (2017), Formation mechanisms of neutral Fe layers in the thermosphere at Antarctica studied with a thermosphere-ionosphere Fe/Fe⁺ (TIFe) model, *J. Geophys. Res. Space Physics*, 122, 6812–6848, doi:10.1002/2016JA023773.

Received 4 DEC 2016

Accepted 9 MAY 2017

Accepted article online 11 MAY 2017

Published online 27 JUN 2017

Formation mechanisms of neutral Fe layers in the thermosphere at Antarctica studied with a thermosphere-ionosphere Fe/Fe⁺ (TIFe) model

Xinzhao Chu¹  and Zhibin Yu¹

¹Cooperative Institute for Research in Environmental Sciences and Department of Aerospace Engineering Sciences, University of Colorado Boulder, Boulder, Colorado, USA

Abstract With a thermosphere-ionosphere Fe/Fe⁺ (TIFe) model developed from first principles at the University of Colorado, we present the first quantitative investigation of formation mechanisms of thermospheric Fe layers observed by lidar in Antarctica. These recently discovered neutral metal layers in the thermosphere between 100 and 200 km provide unique tracers for studies of fundamental processes in the space-atmosphere interaction region. The TIFe model formulates and expands the TIFe theory originally proposed by Chu et al. that the thermospheric Fe layers are produced through the neutralization of converged Fe⁺ layers. Through testing mechanisms and reproducing the 28 May 2011 event at McMurdo, we conceive the lifecycle of meteoric metals via deposition, transport, chemistry, and wave dynamics for thermospheric Fe layers with gravity wave signatures. While the meteor injection of iron species is negligible above 120 km, the polar electric field transports metallic ions Fe⁺ upward from their main deposition region into the *E-F* regions, providing the major source of Fe⁺ (and accordingly Fe) in the thermosphere. Atmospheric wave-induced vertical shears of vertical and horizontal winds converge Fe⁺ to form dense Fe⁺ layers. Direct electron-Fe⁺ recombination is the major channel to neutralize Fe⁺ layers to form Fe above ~120 km. Fe layer shapes are determined by multiple factors of neutral winds, electric field, and aurora activity. Gravity-wave-induced vertical wind plays a key role in forming gravity-wave-shaped Fe layers. Aurora particle precipitation enhances Fe⁺ neutralization by increasing electron density while accelerating Fe loss via charge transfer with enhanced NO⁺ and O₂⁺ densities.

Plain Language Summary The discoveries of neutral metal layers reaching near 200 km in the thermosphere have significant scientific merit because such discoveries challenge the current understandings of upper atmospheric composition, chemistry, dynamics, electrodynamics, and energetics. Furthermore, these neutral metal layers provide tracers for direct measurements of the neutral properties in the least understood but crucially important space-atmosphere interaction region in the altitude range of 100–200 km. With a thermosphere-ionosphere Fe/Fe⁺ (TIFe) model developed from first principles at the University of Colorado, we present the first quantitative investigation of formation mechanisms of thermospheric Fe layers observed by lidar in Antarctica. The TIFe model formulates the TIFe theory depicting the lifecycle of meteoric metals via deposition, transport, chemistry, and wave dynamics. Antarctic lidar observations were successfully reproduced with the TIFe model simulations. These TIFe layers provide a unique natural laboratory for understanding the fundamental processes critical to advancing the research of space-atmosphere interactions.

1. Introduction

The discoveries of neutral metal layers reaching near 200 km in the thermosphere have significant scientific merit because such discoveries challenge the current understandings of upper atmospheric composition, chemistry, dynamics, electrodynamics, and energetics. Furthermore, these neutral metal layers provide tracers for direct measurements of the neutral properties in the least understood but crucially important space-atmosphere interaction region in the altitude range of 100–200 km. Chu et al. [2011] report for the first time lidar observations of neutral Fe layers reaching over 155 km at McMurdo (77.8°S, 166.7°E), Antarctica. Following this, more observations of thermospheric metal layers have been reported from low to high latitudes. For example, a thermospheric neutral K layer up to 155 km was observed descending with a phase

speed compatible with the semidiurnal thermal tide at Arecibo (18.35°N, 66.75°W), Puerto Rico [Friedman *et al.*, 2013]; converged neutral Fe layers descend from at least 140 km or higher at the nearly fixed time every day with a diurnal tidal period at Davis (68.56°S, 77.96°E), Antarctica [Lübken *et al.*, 2011]; descending neutral Na layers have been observed up to 140 km at Syowa (69.0°S, 39.6°E), Antarctica [Tsuda *et al.*, 2015] and up to 130 km at Beijing (40.2°N, 116°E) and Lijiang (26.7°N, 100.0°E), China [Wang *et al.*, 2012; Xue *et al.*, 2013]. Recently, neutral Fe layers have been found reaching over 170 km at McMurdo [Chu *et al.*, 2013, 2016], and neutral Na layers have been observed up to 170 km at Lijiang [Gao *et al.*, 2015] and Cerro Pachón (33.2°S, 70.7°W), Chile [Smith and Chu, 2015]. These metal layers make direct and range-resolved measurements of neutral temperatures in the thermosphere 100–200 km possible, as has been demonstrated up to 170 km at McMurdo using the Fe Boltzmann lidar technique [Chu *et al.*, 2011, 2013, 2016]. With modern Doppler lidar techniques, it has been anticipated that neutral winds in the thermosphere can also be directly measured using the resonance fluorescence excited from such metal layers. In fact, some preliminary results of neutral winds have been demonstrated up to ~140 km using the Na Doppler lidar technique at Cerro Pachón [Liu *et al.*, 2016]. Unfortunately, we still know very little about these metal layers beyond the qualitative explanations provided by Chu *et al.* [2011]. Therefore, there are compelling reasons to significantly further the understanding with numerical simulations and quantitative investigations, which is the subject of this study.

The thermosphere-ionosphere Fe/Fe⁺ (TIFe) theory originally proposed by Chu *et al.* [2011] hypothesizes that thermospheric Fe layers are formed through the neutralization of vertically converged Fe⁺ layers that descend in height, following the downward phase progression of a gravity wave. They further propose that the direct recombination of Fe⁺ with an electron (Fe⁺ + e⁻ → Fe + hν) is the main mechanism that converts Fe⁺ to Fe during the dark polar night at thermospheric altitudes above 120 km, and furthermore, that geomagnetic activity like aurora may have played roles in the observed events at McMurdo [Chu *et al.*, 2011]. This theory of layered metal ions neutralized to form neutral atomic layers has been adapted to describe the thermospheric K layer observed at Arecibo by radiative electron recombination with K⁺ within a tidal ion layer descending with the downward phase progression of the semidiurnal tide [Friedman *et al.*, 2013]. It was also adapted to explain the thermospheric Na layers observed at Syowa [Tsuda *et al.*, 2015] and Lijiang [Gao *et al.*, 2015]. A main reason of invoking the layered metal ions is the extremely high contrast of the observed neutral layers, where the ratios of the wave crest and trough are far larger than any perturbations in the neutral atmosphere [Chu *et al.*, 2011]. Such features distinguish these layers from weak diffusive metal layers extending up to 130 km [Höffner and Friedman, 2005]. The very high altitudes, large vertical range spans, and repeatable gravity wave signatures also distinguish the TIFe layers from sporadic neutral metal layers occurring below 110 km with a width of under a few kilometers but without clear wave signatures (see reviews by Plane [2003] and Plane *et al.* [2015]). We are particularly interested in the thermospheric Fe layer event observed on 28 May 2011 at McMurdo [Chu *et al.*, 2011] because of its intriguing features and the fact that a coronal mass ejection (CME) encountered the Earth as a magnetic cloud on the same day [Li *et al.*, 2014]. The thermospheric Fe layers observed exhibit clear gravity wave features with downward phase progression and a wave period of ~1.5 h. The vertical wavelength increases from ~13 km at 110 km to ~70 km at 150 km. The thermospheric Fe densities are ~20 cm⁻³ at 150 km but exhibit a maximum of ~120 cm⁻³ around 125 km. From ~12 to ~20 UT the Fe layers occur repeatedly for at least five times, and the maximum layer height of each occurrence changes from ~130 km at 12 UT to the highest ~155 km near 15 UT and then decrease to ~125 km at 18.5 UT. The contrast of Fe densities between the wave crests and troughs is very high.

The presence of Fe⁺ ion layers in the *E-F* regions with sufficiently high density is required in Chu *et al.* [2011] to produce detectable neutral Fe atoms through neutralization of Fe⁺. However, it is known that there is no permanent presence of Fe⁺ ions at such high altitudes because meteor ablation and sputtering is insufficient to produce appreciable Fe⁺ or Fe densities in this region [Vondrak *et al.*, 2008; Carrillo-Sánchez *et al.*, 2016] and these heavy ions will sediment under gravitational force. Therefore, the questions raised by Chu *et al.* [2011] include the following:

1. Fe⁺ transport and layering: How are Fe⁺ ions transported into the *E-F* regions and how are Fe⁺ ions converged to form dense layers in the polar region?
2. Fe⁺ neutralization: What are the conversion mechanisms from Fe⁺ to Fe and what roles does aurora particle precipitation play in such conversion?

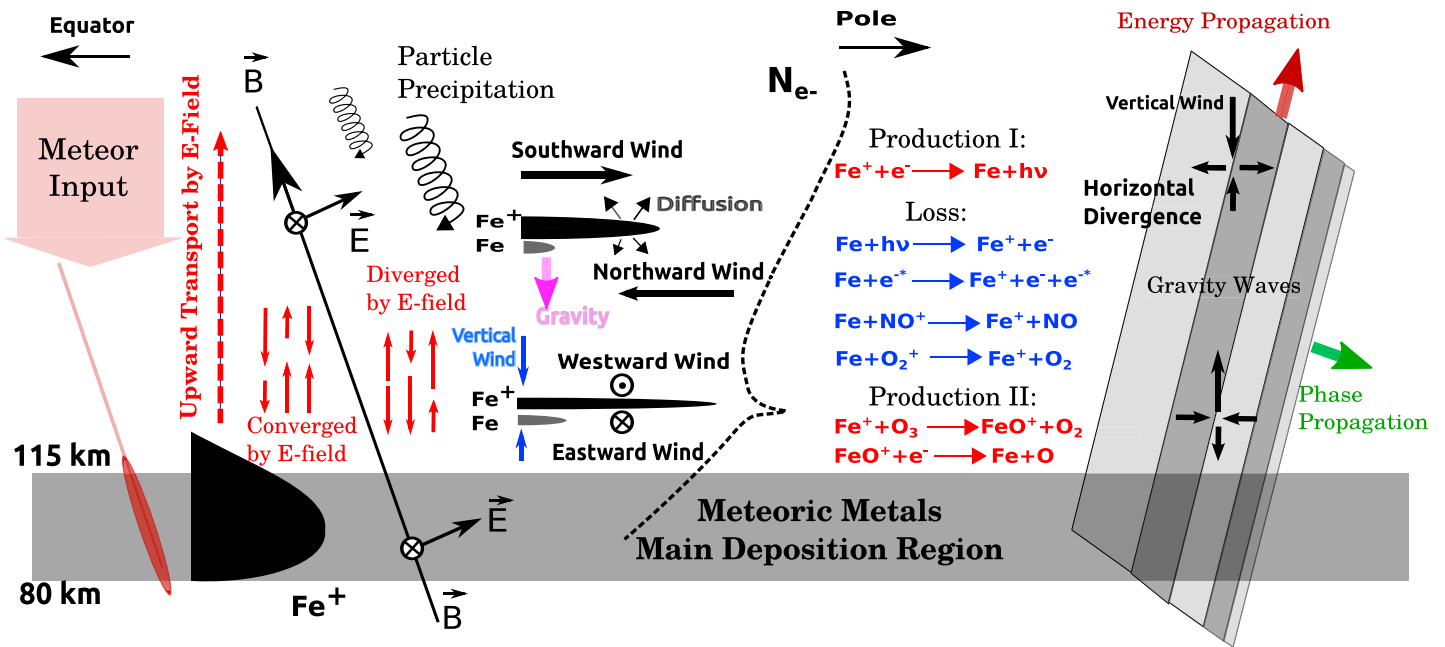


Figure 1. Illustration of physical mechanisms and processes included in the TIFe model that explores the formation theory of thermosphere-ionosphere Fe and Fe⁺ layers in Antarctica. The TIFe theory depicts a full picture of the lifecycle of meteoric metallic ions and atoms via deposition, transport, chemistry, and wave dynamics. The schematic, inspired by *Grebowsky and Pharo* [1985], should be read from left to right.

3. Evolution of Fe layer shapes: What factors determine the Fe layer shapes and why do the observed Fe layers follow gravity wave phases so closely?
4. Energetics of the thermosphere: What processes cause the observed elevated temperatures and temperature inversions, and what roles does geomagnetic activity play?

In this study we aim to investigate questions 1–3 by developing the first thermosphere-ionosphere Fe/Fe⁺ model for the polar region and to simulate the event on 28 May 2011. The “first” refers to the first model simulating thermospheric neutral Fe layers while numerous other models only deal with Fe⁺ ions or deal with Fe and Fe⁺ at lower altitudes.

By expanding and quantifying the original proposal of *Chu et al.* [2011], this study formulates the TIFe theory into a full picture of the lifecycle of meteoric metallic ions and atoms. The physical processes involved in the TIFe theory are illustrated in Figure 1, where the schematic diagram is read from left to right. Meteoric input deposits Fe⁺ and Fe mainly below 115 km. Polar electric fields in favorable directions can transport Fe⁺ ions upward from the main deposition region into the E and F regions. At such high altitudes, the Fe⁺ ions are converged by gravity-wave-induced neutral wind shears under geomagnetic fields to form the dense Fe⁺ layers. While various chemical reactions are involved, it is found that the main neutralization channel is the direct recombination (Fe⁺ + e⁻ → Fe + hν) as proposed in *Chu et al.* [2011], and aurora particle precipitation helps the conversion from Fe⁺ to Fe via enhanced electron densities. Both gravitational force and diffusion contribute to the transport of Fe⁺ and Fe. Gravity waves induce not only the neutral wind shears to converge Fe⁺ layers but also the vertical winds to transport Fe atoms in the thermosphere, once they have been converted from Fe⁺, thus forming the observed gravity wave shapes in Fe layers.

It is worth mentioning that this TIFe theory is inspired by the ion-molecule chemistry theory for sporadic neutral metal layers [*Collins et al.*, 2002; *Plane et al.*, 2003; *Delgado et al.*, 2012] and uses chemistry similar to that of sporadic metal or sporadic E layers. Nevertheless, the TIFe theory possesses its own distinct features. First, the TIFe theory depicts a full picture of the lifecycle of meteoric metallic ions and atoms without presuming a “sea” of metal ions in the E and F regions. Second, the TIFe theory emphasizes the transport of both Fe⁺ ions and Fe atoms, as well as the chemical conversions between them, contrasting previous theories that stress some of these aspects. Third, the TIFe theory demonstrates the importance of direct recombination of electrons with atomic ions Fe⁺ in the middle and upper thermosphere. The converged Fe⁺ layers

hypothesized by *Chu et al.* [2011] are expected to share the same mechanisms as traveling ionospheric disturbances, sporadic *E* layers, and intermediate layers at high latitudes. For the sake of studying sporadic *E* layers or intermediate layers, numerous modeling studies focus on the mechanism of converged ion layers in the *E-F* region (90–250 km) [*MacLeod et al.*, 1975; *Mathews and Bekeny*, 1979; *Bristow and Watkins*, 1991; *Osterman et al.*, 1994; *Carter and Forbes*, 1999; *MacDougall et al.*, 2000; *Bishop and Earle*, 2003]. These numerical simulations support the early theories of forming thin ionization layers in the *E-F* region [*Whitehead*, 1961; *Axford*, 1963; *Nygrén et al.*, 1984]. That is, the converged ion layers are driven by appropriately directed wind shears in combination with the geomagnetic fields or by strong electric fields with appropriate directions. Although the chemistry of metallic ions was embedded into some of the models [e.g., *Carter and Forbes*, 1999; *MacDougall et al.*, 2000; *Bishop and Earle*, 2003], the formation of neutral metal atoms and related layering phenomena in the thermosphere was beyond their scope due to the lack of neutral layer observations. Nevertheless, these previous modeling studies provide the basis for the development of a new Fe/Fe⁺ model in this study.

Indeed, our model framework is based on *Carter and Forbes* [1999]. Equipped with modern computing capabilities and science progress in the past two decades, we are able to significantly improve all modules inside the model and input parameters to the model. The model domain is also changed from low latitudes (for Arecibo) to the polar region (for McMurdo). A description of this new thermosphere-ionosphere Fe/Fe⁺ (TIFe) model is given in section 2, along with a detailed treatment of ion and neutral motions as well as Fe and Fe⁺ chemistry. We then investigate Fe⁺ transport and layering in section 3. Our simulations reveal the important roles of the polar electrical field and wave-induced vertical wind in transporting Fe⁺ ions from their main deposition region to the *E* and *F* regions and in converging Fe⁺ layers in the polar region. Neutralization chemistry to convert Fe⁺ to Fe is studied in section 4. Direct Fe⁺-electron recombination, dissociative recombination, and the roles of aurora in conversion are quantified with the model. Section 5 is devoted to simulations of the thermospheric Fe layer event on 28 May 2011 at McMurdo and investigates the relative importance of multiple factors in forming this impressive event. An overall physical picture of neutral Fe layer formation at thermospheric altitudes is provided in section 6.

2. Thermosphere-Ionosphere Fe/Fe⁺ (TIFe) Model for the Polar Region

The University of Colorado thermosphere-ionosphere Fe/Fe⁺ (TIFe) model is based on a three-dimensional (3-D) mathematical model that starts with the continuity equations of Fe and Fe⁺. The density changes of Fe and Fe⁺ in a volume element fixed in a Cartesian coordinate frame are caused by three mechanisms: source input (meteor ablation and sputtering), chemical production and loss, and transport of Fe and Fe⁺. This understanding forms the basis for the continuity equation (1) that describes the time-changing rates of the number densities of Fe and Fe⁺ in an Eulerian control volume [*Carter and Forbes*, 1999; *MacDougall et al.*, 2000]:

$$\frac{\partial N_M}{\partial t} = S + Q_M - L_M - \nabla \cdot (N_M \vec{V}_M) \quad (1)$$

where *M* represents the minor neutral or ionic species such as Fe or Fe⁺, $N_M(x, y, z, t)$ is the number density of species *M*, which is a function of space and time, *S* is the ultimate external source, *Q* and *L* are respectively the chemical production and loss, and \vec{V}_M is the transport velocity of species *M*. The last term of equation (1) is the divergence of constituent flux of species *M*, representing the constituent transport. Considering the important influences on Fe and Fe⁺ by their transport and chemistry, six more species (FeO⁺, FeO₂⁺, FeN₂⁺, NO⁺, O₂⁺, and O⁺) are also modeled with six separate continuity equations. Note that this 3-D mathematical model is built upon geomagnetic coordinates; i.e., the geomagnetic east (*X*), geomagnetic north (*Y*), and vertical (*Z*) directions are designated as zonal, meridional, and vertical directions in a right-handed coordinate system with vertical up being positive. By projecting the 3-D solutions to the vertical direction, we construct the one-dimensional (1-D) numerical TIFe model along altitude. Detailed development of this Fe/Fe⁺ model was accomplished and documented via a University of Colorado PhD dissertation [*Yu*, 2014]. It is now formally named the TIFe model. Here we briefly describe the physical and chemical basis of the TIFe model, the numerical framework, and further development suitable for the current studies.

2.1. Ultimate Source of Fe and Fe⁺ in the Mesosphere and Thermosphere

The ultimate source of Fe and Fe⁺ in the upper atmosphere is extraterrestrial, i.e., meteoric deposition via ablation and sputtering of meteoroids. Cosmic dust particles enter the Earth's atmosphere at high speeds ranging from 11 to 72 km/s and produce permanent layers of metal species such as Fe, Mg, Na, and K in the mesosphere and lower thermosphere (~75–115 km) [Plane, 2012]. However, above ~120 km where the atmosphere number density is too low to have sufficient friction or sputtering, the meteoric injection rate is too small to sustain any permanent metal layers. This is because such a small injection rate cannot compete against downward transport, especially for heavy metals like Fe and Fe⁺. Plane and coworkers have developed a meteoric Chemical Ablation Model (CABMOD) to calculate the meteor ablation and sputtering from the first principles of physics and chemistry [Vondrak et al., 2008; Feng et al., 2013; Carrillo-Sánchez et al., 2015; Plane et al., 2015]. (The term ablation in CABMOD covers both sputtering and evaporation from the melt [Carrillo-Sánchez et al., 2015].) Combined with meteor input flux (MIF) models, they have modeled the injection rates of metal species along altitude [Vondrak et al., 2008; Feng et al., 2013; Carrillo-Sánchez et al., 2015], considering the distributions of meteoroid mass, velocity, and direction, relative abundance of metal species in meteoroids and ablated vapor, etc. The results show negligible injection rates above ~120 km for three possible MIF distributions derived from Zodiacal cloud observations, Long Duration Exposure Facility, and high-power large-aperture radar observations, respectively [Carrillo-Sánchez et al., 2015]. To provide a quantitative concept, we take the latest calculation results from Carrillo-Sánchez et al. [2016], which give the Fe injection rates of about 1.7×10^{-5} , 3.2×10^{-6} , 4.9×10^{-7} , and $5.0 \times 10^{-8} \text{ cm}^{-3} \text{ s}^{-1}$ at respectively 125, 150, 200, and 300 km for the Planck distribution. Then we compute the average Fe densities for 1 day of continuous accumulation without any loss by downward transport. Note that Fe atoms cannot sustain at such high altitudes for more than a day (see Figure 11 in section 4). The resulting absolute Fe densities are respectively 1.5, 0.28, 0.04, and 0.004 cm^{-3} at these four altitudes. For comparison, the lidar-observed absolute Fe densities are ~120 and 20 cm^{-3} at 125 and 150 km, respectively [Chu et al., 2011], which are about 2 orders of magnitude higher than the direct deposition. Therefore, we conclude that there would not be sufficient Fe or Fe⁺ number densities at observed thermospheric altitudes if transport from the main (permanent) layer were excluded.

Accordingly, the ultimate source input of Fe and Fe⁺ for the simulations of 28 May 2011 event is treated in our model as two initial density profiles of Fe and Fe⁺, instead of continuous input. This is reasonable as the model simulations are for relatively short time periods (~12 h); thus, the meteor input is very minor compared to the mean background profiles of Fe and Fe⁺ densities as argued below. The mean density distributions of Fe and Fe⁺ are determined, to the first-order approximation, by the product of the mean injection rates and the mean lifetimes of Fe species in the mesosphere and lower thermosphere (MLT) region. Such mean densities should match observations of Fe and Fe⁺ densities, regardless of the very large uncertainty (ranging from 2 to 300 t/d) currently associated with the total meteor input flux [Plane, 2012; Feng et al., 2013; Gardner et al., 2014; Huang et al., 2015]. It is clear that injection rates above 120 km are significantly smaller (about 4 orders of magnitude) than those in the main deposition region below 110 km [Vondrak et al., 2008; Feng et al., 2013]. If taking the injection rates estimated by Vondrak et al. [2008] for ~88 t/d meteor influx, the injection rates above 120 km are about or less than $10 \text{ m}^{-3} \text{ s}^{-1} = 10^{-5} \text{ cm}^{-3} \text{ s}^{-1}$. It would then require at least $10^5 \text{ s} = 27.8 \text{ h}$ for the entire Fe species to accumulate a density of 1 cm^{-3} above 120 km, even without considering the downward transport loss caused by gravity and atmospheric waves. Therefore, meteor injection above 120 km over a 12–24 h interval is negligible compared to the Fe⁺ density (~ 10^5 cm^{-3}) required to produce the observed Fe density (~10–100 cm^{-3}) above 120 km.

We are aware of a debate in the community that sputtering of very fast meteoroids (with entry velocities >60 km/s) may cause the injection rates at high altitudes to be much larger than those quoted above [Popova et al., 2007]. Since such fast meteoroids only make up a tiny fraction of the cosmic dust entering the Earth [Carrillo-Sánchez et al., 2016] and there is currently no direct observational data of sputtering, we choose not to include these rare events in our model. Instead, we will demonstrate in this study that the upward transport of Fe⁺ ions under normal meteor deposition conditions is sufficient to reproduce the lidar-observed TIFE layers.

Table 1. Neutral and Ionic Gas-Phase Chemistry of Iron Species (Fe and Fe⁺) in the TIFE Model

Reaction Number	Reaction	Rate Coefficient ^a	Reference
R1	Fe ⁺ + e ⁻ → Fe + hν	$k_1 = 6.59 \times 10^{-12} (T/300)^{-0.50}$	Nahar et al. [1997]
R2	Fe ⁺ + O ₃ → FeO ⁺ + O ₂	$k_2 = 7.07 \times 10^{-10} \exp(-129.9/T)$	Rollason and Plane [1998]
R3	FeO ⁺ + e ⁻ → Fe + O	$k_3 = 5.5 \times 10^{-7} \sqrt{298/T}$	Bones et al. [2016]
R4	FeO ⁺ + O → Fe ⁺ + O ₂	$k_4 = 3.2 \times 10^{-11}$	Woodcock et al. [2006]
R5	Fe + hν → Fe ⁺ + e ⁻	$k_5 = 5 \times 10^{-7} [s^{-1}]^b$	Bautista et al. [1998]
R6	Fe + e ^{-*} → Fe ⁺ + e ⁻ + e ^{-*}	See Text	Shah et al. [1993]
R7	Fe + O ₂ ⁺ → Fe ⁺ + O ₂	$k_7 = 1.1 \times 10^{-9}$	Rutherford and Vroom [1972]
R8	Fe + NO ⁺ → Fe ⁺ + NO	$k_8 = 9.2 \times 10^{-10}$	Rutherford and Vroom [1972]
R9	Fe + O ₃ → FeO + O ₂	$k_9 = 3.44 \times 10^{-10} \exp(-145.5/T)$	Helmer and Plane [1994]
R10	FeO + O → Fe + O ₂	$k_{10} = 4.6 \times 10^{-10} \exp(-350/T)$	Self and Plane [2003]
R11	FeN ₂ ⁺ + O → FeO ⁺ + N ₂	$k_{11} = 4.6 \times 10^{-10}$	Woodcock et al. [2006]
R12	FeO ₂ ⁺ + O → FeO ⁺ + O ₂	$k_{12} = 6.3 \times 10^{-11}$	Woodcock et al. [2006]
R13	FeO ₂ ⁺ + e ⁻ → Fe + O ₂	$k_{13} = 3 \times 10^{-7} \sqrt{200/T}$	Helmer et al. [1998]
R14	FeN ₂ ⁺ + e ⁻ → Fe + N ₂	$k_{14} = 3 \times 10^{-7} \sqrt{200/T}$	Plane et al. [1999]
R15	Fe ⁺ + N ₂ + M → FeN ₂ ⁺ + M	$k_{15} = 8.0 \times 10^{-30} (T/300)^{-1.52}$	Woodcock et al. [2006]
R16	Fe ⁺ + O ₂ + M → FeO ₂ ⁺ + M	$k_{16} = 1.7 \times 10^{-29} (T/300)^{-1.86}$	Woodcock et al. [2006]
R17	FeN ₂ ⁺ + O ₂ → FeO ₂ ⁺ + N ₂	$k_{17} = 3.17 \times 10^{-10}$	Vondrak et al. [2006]
R18	FeO + O ₃ → FeO ₂ + O ₂	$k_{18} = 2.94 \times 10^{-10} \exp(-174.4/T)$	Rollason and Plane [2000]
R19	FeO + O ₂ + M → FeO ₃ + M	$k_{19} = 4.41 \times 10^{-30} (T/200)^{0.606}$	Rollason and Plane [2000]
R20	FeO ₂ + O → FeO + O ₂	$k_{20} = 1.4 \times 10^{-10} \exp(-580/T)$	Self and Plane [2003]
R21	FeO ₂ + O ₃ → FeO ₃ + O ₂	$k_{21} = 4.4 \times 10^{-10} \exp(-170/T)$	Self and Plane [2003]
R22	FeO ₃ + O → FeO ₂ + O ₂	$k_{22} = 3.5 \times 10^{-10} \exp(-2386/T)$	Self and Plane [2003]
R23	FeO ₃ + H ₂ O → Fe(OH) ₂ + O ₂	$k_{23} = 5.0 \times 10^{-12}$	Self and Plane [2003]
R24	FeO + H ₂ O + M → Fe(OH) ₂ + M	$k_{24} = 5 \times 10^{-28} (200/T)^{1.13}$	Rollason and Plane [2000]
R25	Fe(OH) ₂ + H → FeOH + H ₂ O	$k_{25} = 1.1 \times 10^{-10} \exp(-300/T)$	Jensen and Jones [1974]
R26	FeO ₃ + H → FeOH + O ₂	$k_{26} = 3 \times 10^{-10} \exp(-796/T)$	Feng et al. [2013]
R27	FeOH + H → Fe + H ₂ O	$k_{27} = 2.0 \times 10^{-12} \exp(-600/T)$	Jensen and Jones [1974]
R28	FeOH + H → FeO + H ₂	$k_{28} = 5.0 \times 10^{-11} \exp(-800/T)$	Jensen and Jones [1974]
R29	FeOH + FeOH → (FeOH) ₂	$k_{29} = 9 \times 10^{-10}$	Feng et al. [2013]
R30	FeOH + hν → Fe + OH	$k_{30} = 6 \times 10^{-3} [s^{-1}]^b$	Viehl et al. [2016]
R31	Fe + O ⁺ → Fe ⁺ + O	$k_{31} = 2.94 \times 10^{-9}$	Rutherford and Vroom [1972]
R32	Fe + N ⁺ → Fe ⁺ + N	$k_{32} = 1.47 \times 10^{-9}$	Rutherford and Vroom [1972]
R33	Fe + N ₂ ⁺ → Fe ⁺ + N ₂	$k_{33} = 4.29 \times 10^{-10}$	Rutherford and Vroom [1972]
R34	Fe + H ⁺ → Fe ⁺ + H	$k_{34} = 7.35 \times 10^{-9}$	Rutherford and Vroom [1972]

^aThe unit of rate coefficient is cm³ s⁻¹ for bimolecular reactions and cm⁶ s⁻¹ for termolecular reactions.

^bWhen the solar elevation angle is below 0°, k₅ and k₃₀ are zero.

2.2. Chemical Production and Loss of Fe and Fe⁺

The atomic Fe and Fe⁺ released from meteoric ablation undergo complex chemistry. A schematic diagram of the recently updated Fe and Fe⁺ chemistry in the mesosphere and lower thermosphere (MLT) is given in Plane [2012] and Plane et al. [2015]. The reactions of Fe and Fe⁺ with ambient neutral species (like O, O₂, O₃, N, N₂, NO, H, H₂O, and CO₂, etc.) and ionic species (like NO⁺, O₂⁺, and O⁺, etc.) produce neutral and ionic iron molecules (like FeO, FeO₂, FeO₃, FeOH, Fe(OH)₂, FeO⁺, FeO₂⁺, and FeN₂⁺, etc.). The dynamical systems of reactions among Fe, Fe⁺, molecular iron species, photons, and precipitation electrons produce the chemical production and loss of Fe and Fe⁺. All iron species-related reactions (34) considered in the TIFE model are listed in Table 1, along with their reaction rate coefficients. In the thermosphere above ~120 km and in the polar region, several extra reactions, normally not considered in the mesospheric iron chemistry but included in Table 1, are the direct recombination of Fe⁺ with electron (R1), photoionization of Fe (R5), ionization of Fe by energetic electron impact (R6), and charge transfers of Fe with O⁺, N⁺, N₂⁺, and H⁺ (R31–R34). Most of the reaction rate coefficients used in the Fe/Fe⁺ chemistry are from the laboratory measurements by Plane and coworkers in recent decades, including the newest result on dissociative recombination rate k₃ [Bones et al., 2016]. The reaction rate coefficient k₁ for the direct recombination (R1), which is essential to this study, is taken from Nahar et al. [1997] as a quantum mechanics computational

result. The reaction rate coefficient for (R6) is taken from *Shah et al.* [1993] and further derived in this study (see section 4.2). The rate coefficients for six charge transfers (R7, R8, and R31–R34) are taken from *Rutherford and Vroom* [1972].

Based on the Fe/Fe⁺ chemistry [*Plane et al.*, 2003; *Plane*, 2012; *Feng et al.*, 2013; *Plane et al.*, 2015] and related molecular ion reactions, we choose to model 16 minor species in our chemical module, which are defined in the constituent array CA = (Fe, Fe⁺, FeO, FeO⁺, FeO₂, FeO₂⁺, FeO₃, FeN₂⁺, FeOH, Fe(OH)₂, NO⁺, O₂⁺, O⁺, N₂⁺, N⁺, and N). These 16 minor species include all iron-containing species along with five major ions (NO⁺, O₂⁺, O⁺, N₂⁺, and N⁺) and neutral N, except FeOOH, FeCO₃, and the dimer sink (FeOH)₂. The time change rates of the 16 minor species, due to chemical reactions, are governed by 16 ordinary differential equations (ODEs). Two examples are given below:

$$\begin{aligned} \frac{d[\text{Fe}]}{dt} = & k_1[\text{Fe}^+][e^-] + k_3[\text{FeO}^+][e^-] - k_5[\text{Fe}][h\nu] - k_6[\text{Fe}][e^*] - k_7[\text{Fe}][\text{O}_2^+] - k_8[\text{Fe}][\text{NO}^+] \\ & - k_9[\text{Fe}][\text{O}_3] + k_{10}[\text{FeO}][\text{O}] + k_{13}[\text{FeO}_2^+][e^-] + k_{14}[\text{FeN}_2^+][e^-] + k_{27}[\text{FeOH}][\text{H}] \\ & + k_{30}[\text{FeOH}][h\nu] - k_{31}[\text{Fe}][\text{O}^+] - k_{32}[\text{Fe}][\text{N}^+] - k_{33}[\text{Fe}][\text{N}_2^+] - k_{34}[\text{Fe}][\text{H}^+] \end{aligned} \quad (2)$$

and

$$\begin{aligned} \frac{d[\text{Fe}^+]}{dt} = & -k_1[\text{Fe}^+][e^-] - k_2[\text{Fe}^+][\text{O}_3] + k_4[\text{FeO}^+][\text{O}] + k_5[\text{Fe}][h\nu] + k_6[\text{Fe}][e^*] \\ & + k_7[\text{Fe}][\text{O}_2^+] + k_8[\text{Fe}][\text{NO}^+] - k_{15}[\text{Fe}^+][\text{N}_2][M] - k_{16}[\text{Fe}^+][\text{O}_2][M] \\ & + k_{31}[\text{Fe}][\text{O}^+] + k_{32}[\text{Fe}][\text{N}^+] + k_{33}[\text{Fe}][\text{N}_2^+] + k_{34}[\text{Fe}][\text{H}^+] \end{aligned} \quad (3)$$

Here the reaction rate coefficients k_i are given in Table 1. In the chemical module of TIFE model, the 10 iron species fulfill the mass conservation law. That is, the total number density of iron species is conservative in the absence of transport and external source, which is expressed as

$$\begin{aligned} \frac{d[\text{Fe}]}{dt} + \frac{d[\text{Fe}^+]}{dt} + \frac{d[\text{FeO}]}{dt} + \frac{d[\text{FeO}^+]}{dt} + \frac{d[\text{FeO}_2]}{dt} + \frac{d[\text{FeO}_2^+]}{dt} \\ + \frac{d[\text{FeN}_2^+]}{dt} + \frac{d[\text{FeO}_3]}{dt} + \frac{d[\text{FeOH}]}{dt} + \frac{d[\text{Fe(OH)}_2]}{dt} = 0 \end{aligned} \quad (4)$$

Fe and Fe⁺ chemistry in the thermosphere is heavily influenced by ambient molecular ions. The chemical reactions of molecular ions NO⁺, O₂⁺, O⁺, N₂⁺, and N⁺ considered in the model are listed in Table 2 along with corresponding reaction rate coefficients. Also listed are three photoionization reactions for major neutral species N₂, O₂, and O. It is worth pointing out that both the neutral chemistry and the photochemical process of FeOH are included in the TIFE model (see Table 1). Among them, the photolysis rate of FeOH has been updated to the latest results obtained from quantum chemical calculations and Fe model-observation comparisons by *Plane and colleagues* [*Viehl et al.*, 2016]. Because the thermospheric Fe layer event of 28 May 2011 occurred during a dark polar night, sunlight was absent at all altitudes concerned. Consequently, the photon flux is set to zero in this study.

2.3. Transport of Fe and Fe⁺

Besides the source input and chemical production and loss, transport due to motions of Fe and Fe⁺ contributes to the time-changing rates of Fe and Fe⁺ via the divergence term in equation (1). Moreover, transport of minor species other than Fe and Fe⁺, as discussed in section 2.2, can also affect Fe and Fe⁺ by varying the concentrations of these minor species in the chemical production and loss of Fe and Fe⁺. Therefore, the transport module must “track” these important species in addition to Fe and Fe⁺. In the TIFE model, constituent transport is considered for neutral Fe and seven ion species (Fe⁺, FeO⁺, FeO₂⁺, FeN₂⁺, NO⁺, O₂⁺, and O⁺) via eight full continuity equations. The other eight minor species modeled by ODEs in the chemical module, including six neutral species (FeO, FeO₂, FeO₃, FeOH, Fe(OH)₂, and N) and two ion species (N₂⁺ and N⁺), are not modeled for their transport. This choice of modeling is based on several considerations. First, according to the TIFE theory by *Chu et al.* [2011], the formation of Fe layers in the thermosphere is mainly related to Fe⁺ layers, involving ionic transport driven by electromagnetic fields and neutral dynamics. It is thus important to track all iron-containing ions and three

Table 2. Molecular Ion Reactions and Photoionization Reactions in the TIFe Model

Reaction Number	Reaction	Rate Coefficient (cm ³ s ⁻¹)	Reference
R35	NO ⁺ + e ⁻ → N + O	^a k ₃₅ = 4.2 × 10 ⁻⁷ (T _e /300) ^{-0.85}	Vejby-Christensen et al. [1998]
R36	O ₂ ⁺ + e ⁻ → O + O	k ₃₆ = 1.9 × 10 ⁻⁷ (T _e /300) ^{-0.5}	Mul and McGowan [1979]
R37	N ₂ ⁺ + e ⁻ → N + N	k ₃₇ = 3.5 × 10 ⁻⁷ (T _e /300) ^{-0.5}	Mul and McGowan [1979]
R38	O ⁺ + N ₂ → NO ⁺ + N	k ₃₈ = 2.78 × 10 ⁻¹³ exp [2.07(T _f /300) ⁻¹ - 0.61(T _f /300) ⁻²]	Chen et al. [1978]
R39	O ⁺ + O ₂ → O ₂ ⁺ + O	k ₃₉ = 3.33 × 10 ⁻¹² exp [3.72(T _f /300) ⁻¹ - 1.87(T _f /300) ⁻²]	Chen et al. [1978]
R40	O ₂ ⁺ + NO → NO ⁺ + O ₂	k ₄₀ = 4.4 × 10 ⁻¹⁰	Lindinger and Ferguson [1983]
R41	O ₂ ⁺ + N ₂ → NO ⁺ + NO	k ₄₁ = 5.0 × 10 ⁻¹⁶	
R42	N ₂ ⁺ + O → NO ⁺ + N	k ₄₂ = 1.4 × 10 ⁻¹⁰ (600/(T _i + T _n)) ^{0.44}	McFarland et al. [1974]
R43	N ₂ ⁺ + O → O ⁺ + N ₂	k ₄₃ = 1.0 × 10 ⁻¹¹ (600/(T _i + T _n)) ^{0.23}	
R44	N ₂ ⁺ + O ₂ → O ₂ ⁺ + N ₂	k ₄₄ = 6.0 × 10 ⁻¹¹	McFarland et al. [1973]
R45	O ⁺ + CO ₂ → O ₂ ⁺ + CO	k ₄₅ = 1.1 × 10 ⁻⁹	Schunk and Nagy [2009]
R46	O ₂ ⁺ + N → NO ⁺ + O	k ₄₆ = 1.2 × 10 ⁻¹⁰	Fehsenfeld [1977]
R47	N ⁺ + O ₂ → O ₂ ⁺ + N	k ₄₇ = 4.0 × 10 ⁻¹⁰	Langford et al. [1985]
R48	N ⁺ + O ₂ → NO ⁺ + O	k ₄₈ = 2.0 × 10 ⁻¹⁰	Langford et al. [1985]
R49	N ⁺ + O → O ⁺ + N	k ₄₉ = 1.0 × 10 ⁻¹²	Torr [1985]
R50	O ⁺ + NO → NO ⁺ + O	^b k ₅₀ = 8.36 × 10 ⁻¹³ - 2.02 × 10 ⁻¹³ (T _f /300) + 6.95 × 10 ⁻¹⁴ (T _f /300) ²	St.-Maurice and Torr [1978]
R51	O ⁺ + e ⁻ → O + hν	k ₅₁ = 7.8 × 10 ⁻¹⁴ (300/T _e) ^{0.5}	Brekke [2013]
R52	N ₂ + hν → N ₂ ⁺ + e ⁻	GLOW model	Solomon et al. [1988]
R53	N ₂ + e ^{-*} → N ₂ ⁺ + e ⁻ + e ^{-*}	GLOW model	Solomon et al. [1988]
R54	N + hν → N ⁺ + e	GLOW model	Solomon et al. [1988]
R55	N ₂ + hν → N ⁺ + N + e	GLOW model	Solomon et al. [1988]
R56	O ₂ + hν → O ₂ ⁺ + e ⁻	GLOW model	Solomon et al. [1988]
R57	O ₂ + hν → O ⁺ + O + e	GLOW model	Solomon et al. [1988]
R58	O ₂ + e ^{-*} → O ₂ ⁺ + e ⁻ + e ^{-*}	GLOW model	Solomon et al. [1988]
R59	O + hν → O ⁺ + e ⁻	GLOW model	Solomon et al. [1988]
R60	O + e ^{-*} → O ⁺ + e ⁻ + e ^{-*}	GLOW model	Solomon et al. [1988]

^aWhere T_e, T_i, T_n, and T_f are electronic, ionic, neutral, and effective temperatures, respectively.

^b320 < T_f ≤ 1500 K.

major ion species (NO⁺, O₂⁺, and O⁺) in the *E-F* region, which would undergo similar transport as Fe⁺. Second, no mechanisms are known to sufficiently transport neutral metals from the main deposition region (below 120 km) into the *E-F* regions. Aurora heating in the polar region may cause upwelling and thus upward transport constituents into the thermosphere [Burns et al., 1991], but this mechanism is unproven at these low altitudes. Thus, the direct transport of neutral species from the main layer upward is insignificant in this study. Third, due to the lack of O₃ in the thermosphere, neutral reactions about molecular iron species would not happen. Therefore, the transport of neutral species (except neutral Fe) and two minor ion species (N₂⁺ and N⁺) is not considered in this model. Such a choice helps maintain the model stability when the capability of the model is constrained. The electron density in the TIFe model is set to equal the total ion densities in each grid cell in order to maintain the electrical neutrality for every cell.

In contrast to the density changes caused by scalar chemical reactions, transport involves 3-D vector variables such as the ion and neutral velocities, geomagnetic fields, electric fields, and background and wave-induced winds. Our mathematical model solves the 3-D motion equations of Fe⁺ and Fe and obtains the full 3-D solutions of Fe⁺ and Fe motions in the geomagnetic coordinates. The 3-D solutions are then projected to the vertical direction for tracking the vertical transport in the 1-D numerical TIFe model. Here we provide a relatively detailed treatment of Fe⁺ and Fe motions before treating the transport term.

2.3.1. Motions of Fe⁺

Motions of Fe⁺ are governed by electric and magnetic fields, neutral winds through ion-neutral collisions, gravitational force, ionic diffusion, ion-electron collision, and Coriolis force in the frame fixed to the Earth's

surface [Gossard and Hooke, 1975]. The first-order approximation is considered in the TIFE model; i.e., ions are in force balance, and the Coriolis force and the momentum transferred between ions and electrons are negligible. Then the motions of ions in a steady state are governed by the force balance equation (5):

$$q\vec{E} + q\vec{V}_i \times \vec{B} + m_i v_{in} (\vec{V}_n - \vec{V}_i) + m_i \vec{g} - \frac{\nabla P_i}{N_i} = 0 \quad (5)$$

where q , m_i , and \vec{V}_i are the charge, mass, and velocity of an ion, \vec{V}_n is the velocity of the neutral background (i.e., the neutral winds), \vec{E} and \vec{B} are the electric field and magnetic field, v_{in} is the ion-neutral collision frequency, \vec{g} is the gravitational acceleration, N_i is the number density of this ion species, and $P_i = k_B N_i T_i$ is the ionic pressure. Here k_B is the Boltzmann constant and T_i is the ion temperature. In equation (5) the first term is Coulomb force, the second term is Lorentz force, the third term represents neutral-ion collision, the fourth term is gravitational force, and the last term is ionic pressure gradient. We define the sum of the last two terms as $\vec{F}_i = m_i \vec{g} - \frac{\nabla P_i}{N_i}$ in order to simplify the solution of equation (5).

The solution of ion motions is given by equation (6):

$$\begin{aligned} \vec{V}_i = & \frac{1}{1 + \zeta^2} \frac{\vec{E} \times \vec{B}}{B^2} + \frac{q(\vec{E} \cdot \vec{B})}{m_i v_{in} B^2 (1 + \zeta^2)} \vec{B} + \frac{\zeta}{1 + \zeta^2} \frac{\vec{E}}{B} + \frac{\zeta}{1 + \zeta^2} \frac{\vec{V}_n \times \vec{B}}{B} + \frac{1}{1 + \zeta^2} \frac{(\vec{V}_n \cdot \vec{B})}{B^2} \vec{B} + \frac{\zeta^2}{1 + \zeta^2} \vec{V}_n \\ & + \frac{\vec{F}_i \times \vec{B}}{qB^2 (1 + \zeta^2)} + \frac{(\vec{F}_i \cdot \vec{B})}{m_i v_{in} B^2 (1 + \zeta^2)} \vec{B} + \frac{\zeta}{qB (1 + \zeta^2)} \vec{F}_i \end{aligned} \quad (6)$$

where $\zeta = \frac{v_{in}}{\omega_i}$ is the ratio of ion-neutral collision frequency to ion gyrofrequency and $\omega_i = \frac{qB}{m_i}$ is the ion gyrofrequency. By writing the solution in the form of equation (6), it is easy to infer various contributions to the ion motions. The first three terms are contributions by the electric field, the middle three terms are contributions from the neutral winds, and the last three terms are related to contributions by gravity and diffusion. All these contributors contribute to the ion motions through interactions with the magnetic field (the cross B and dot B terms) and by themselves directly (the direct force terms). The first term is the E cross B ion drift, and the third term is the Coulomb-force-induced ion drift along the E direction. The fourth term is the Lorentz-force-induced V cross B drift, the fifth term is the neutral-ion-collision-induced ion motion along the magnetic field line, and the sixth term is the neutral-ion collision moving ions along the neutral wind V_n direction. The $\vec{E} \cdot \vec{B}$ term is not negligible, because it is important for field-aligned diffusion. This term is proportional to the electron pressure gradient along \vec{B} . The electron and ion pressure gradient terms act in the same direction, producing ambipolar diffusion.

By projecting the ion motion's solution equation (6) to the vertical direction z , we obtain the vertical drift velocity of ions V_{iz} . Given in equations (7)–(9), V_{iz} is decomposed into three groups, V_{ize} , V_{izw} , and V_{izgd} , as the vertical drift velocities of ion driven respectively by the electric field, neutral wind, and gravity and diffusion.

$$V_{ize} = \frac{\cos \Theta_D E_x}{1 + \zeta^2 B_0} + \frac{\zeta}{1 + \zeta^2} \frac{E_z}{B_0} \quad (7)$$

$$V_{izw} = \frac{\zeta \cos \Theta_D}{1 + \zeta^2} V_{n,x} - \frac{\sin(2\Theta_D)}{2(1 + \zeta^2)} V_{n,y} + \left(1 - \frac{\cos^2 \Theta_D}{1 + \zeta^2}\right) V_{n,z} \quad (8)$$

$$V_{izgd} = \left[1 - \frac{(\cos \Theta_D)^2}{1 + \zeta^2}\right] \left[-\frac{g}{v_{in}} - \left(\frac{D_i}{N_i}\right) \frac{\partial N_i}{\partial z} - \left(\frac{D_i}{T_i}\right) \frac{\partial T_i}{\partial z}\right] \quad (9)$$

where B_0 is the geomagnetic field strength, Θ_D is the dip angle of geomagnetic field line and $\Theta_D = -80.1^\circ$ at McMurdo, and E_x and E_z are the geomagnetic east-west and vertical components of the ionospheric electric field. $V_{n,x}$, $V_{n,y}$, and $V_{n,z}$ are the neutral wind components in the geomagnetic east, geomagnetic north, and vertical directions, g is the gravitational acceleration, and $D_i = \frac{k_B(T_i + T_e)}{m_i v_{in}}$ is the molecular diffusion coefficient of

ion, where T_e is the electron temperature. Equations (7) and (8) will be analyzed in section 3. In equation (9), the gravity-induced velocity g/v_{in} is small when the ion-neutral collision frequency v_{in} is high. The diffusion terms are related to the vertical gradients of N_i and T_i .

2.3.2. Motions of Fe

Motions of neutral Fe are controlled by neutral atmosphere winds, gravitational force, and diffusion. Since neutral Fe atoms are free of the constraints of electromagnetic forces, we assume that Fe atoms are immediately balanced by neutral background via thermal collisions and follow the motions of the background neutral winds after Fe atoms are formed through neutralization of Fe^+ . Additionally, the vertical transport of Fe in the thermosphere is subject to gravitational force and diffusion. Therefore, the velocity of neutral Fe motions is determined by the sum of three terms in equation (10):

$$\vec{V}_{Fe} = \vec{V}_n + \vec{V}_g + \vec{V}_d \quad (10)$$

where \vec{V}_{Fe} is the total Fe velocity, \vec{V}_n is the neutral wind velocity, and \vec{V}_g and \vec{V}_d are the velocities of Fe caused by gravity and diffusion, respectively.

Following Chapter 3.8 of *Brasseur and Solomon* [2005] and Chapter 15 of *Banks and Kockarts* [1973], the total vertical "diffusion and gravity" velocity $w_{Fe,gd}$, i.e., the vertical projection of the sum of \vec{V}_g and \vec{V}_d , is the sum of vertical "molecular diffusion velocity" $w_{D,Fe}$ and effective vertical "eddy diffusion velocity" $w_{E,Fe}$:

$$w_{Fe,gd} = w_{D,Fe} + w_{E,Fe} \quad (11)$$

The vertical molecular diffusion velocity for Fe can be expressed as [*Banks and Kockarts*, 1973]

$$w_{D,Fe} = -D_{Fe} \left(\frac{1}{N_{Fe}} \frac{\partial N_{Fe}}{\partial z} + \frac{1}{T_N} \frac{\partial T_N}{\partial z} + \frac{1}{H_{Fe}} \right) \quad (12)$$

where N_{Fe} is the number density of Fe, T_N is the neutral atmosphere temperature, $H_{Fe} = k_B T_N / m_{Fe} g$ is the scale height of Fe density, and $D_{Fe} = \frac{k_B T_N}{m_{Fe} v_n}$ is the molecular diffusion coefficient of Fe. Here v_n is the sum of neutral-neutral and neutral-ion collision frequencies for Fe. Formulas to compute neutral-neutral, neutral-ion, and ion-ion collision frequencies were obtained from *Banks and Kockarts* [1973]. The average neutral-neutral collision frequency is given by $v_{n_1 n_2} = n_2 \sigma_0 \bar{V}_{12}$, where n_1 is Fe density, n_2 is the number density of the ambient neutral atmosphere, $\sigma_0 = \pi(r_1 + r_2)^2$ is the collision cross section, and $\bar{V}_{12} = \left(\frac{8k_B T_N}{\pi \mu} \right)^{1/2}$ is the average relative speed. Here r_1 and r_2 are the approximation radii of the colliding particles, and $\mu = \frac{m_1 m_2}{m_1 + m_2}$ is the reduced mass of Fe mass m_1 and ambient particle mass m_2 . Derived from the momentum equation under zero neutral wind background [*Banks and Kockarts*, 1973], $w_{D,Fe}$ includes the contribution of gravity, which is denoted by the scale height term $D_{Fe}/H_{Fe} = g/v_n$.

The vertical eddy diffusion velocity for Fe is expressed as [*Brasseur and Solomon*, 2005; *Banks and Kockarts*, 1973]

$$w_{E,Fe} = -K_Z \left(\frac{1}{N_{Fe}} \frac{\partial N_{Fe}}{\partial z} + \frac{1}{T_N} \frac{\partial T_N}{\partial z} + \frac{1}{H_g} \right) \quad (13)$$

where K_Z is the vertical eddy diffusion coefficient, $H_g = k_B T_N / m_{air} g$ is the atmospheric density scale height, and m_{air} is the mean mass of atmosphere. The vertical eddy diffusion coefficient K_Z in our model is set to the empirical values from *U.S. Standard Atmosphere* [1976], which is $10^6 \text{ cm}^2 \text{ s}^{-1}$ below 100 km, $10^5 \text{ cm}^2 \text{ s}^{-1}$ at 110 km, $10^4 \text{ cm}^2 \text{ s}^{-1}$ at 120 km, and 0 above 120 km. As pointed out by *Banks and Kockarts* [1973], molecular diffusion tends to separate the atmosphere constituents according to their mass, but turbulence tends to mix the atmospheric constituents and in this way prevents any separation by molecular diffusion. While turbulence mixing prevails in the homosphere, diffusive separation occurs in the heterosphere. In the vicinity of the homopause around 100 km, both processes are of the same order of magnitude. Therefore, the effects of both eddy and molecular diffusion have to be taken into account as given by equation (11).

2.3.3. Constituent Transport in the Continuity Equations

The constituent transport is represented as the divergence of constituent number flux, $\nabla \cdot (N_M \vec{V}_M)$, in equation (1), which describes the 3-D constituent flowing into and out of a grid cell. This 3-D divergence term can be decomposed into two terms—the horizontal divergence and the vertical transport:

$$\nabla \cdot (N_M \vec{V}_M) = \nabla_h \cdot (N_M \vec{V}_{M,h}) + \frac{\partial (N_M V_{M,z})}{\partial z} \quad (14)$$

where $\vec{V}_{M,h}$ and $V_{M,z}$ represent the horizontal and vertical transport velocities of species M , respectively. Such a mathematical term requires a 3-D numerical model to fully calculate the divergence of constituent flux, which is impractical for this first attempt of modeling the thermosphere-ionosphere Fe and Fe⁺ layers. The 1-D TIFE model computes the vertical transport $\partial(N_M V_{M,z})/\partial z$ precisely by adopting a high-order flux-corrected transport algorithm, but it does not possess the capability to track the horizontal motions in multiple horizontal cells so it cannot compute the horizontal divergence precisely. A survey of the current literature shows that the most popular approach taken in 1-D modeling is to completely ignore the horizontal divergence term by assuming no significant variations in any horizontal direction [e.g., MacDougall et al., 2000]. Unfortunately, this approach is not applicable to the current study because the vertical convergence to be studied here will automatically induce horizontal divergence in an approximately incompressible atmosphere such as the upper atmosphere. The induced horizontal divergence can largely offset the vertical convergence. Accordingly, the horizontal divergence term is nondismissible for both the neutral and ionic continuity equations in this study.

In our 1-D model we choose to parameterize the horizontal divergence term as follows. Considering $\nabla_h \cdot (N_M \vec{V}_{M,h}) = \nabla_h N_M \cdot \vec{V}_{M,h} + N_M \nabla_h \cdot \vec{V}_{M,h}$, we make an assumption that the horizontal gradient of the constituent number density N_M is negligible, i.e., $\nabla_h N_M \approx 0$. As a result, equation (14) is simplified to

$$\nabla \cdot (N_M \vec{V}_M) \approx \frac{\partial (N_M V_{M,z})}{\partial z} + N_M \nabla_h \cdot \vec{V}_{M,h} \quad (15)$$

The horizontal divergence of the transport velocity, $\nabla_h \cdot \vec{V}_{M,h}$, is then derived in terms of the divergence of neutral horizontal winds ($\nabla_h \cdot \vec{V}_{n,h}$) for the neutral and ionic species. Taking the horizontal divergence of equation (10) and neglecting the horizontal gradients of the gravity- and diffusion-associated velocities, the horizontal divergence for neutral Fe, $\nabla_h \cdot \vec{V}_{Fe,h}$, is equal to the horizontal divergence of horizontal winds of the background atmosphere

$$\nabla_h \cdot \vec{V}_{Fe,h} = \nabla_h \cdot \vec{V}_{n,h} \quad (16)$$

The horizontal divergence term for ionic species like Fe⁺ is evaluated by taking the divergence of equation (6). When only considering the horizontal gradients of the gravity wave-induced horizontal winds while neglecting the horizontal gradients associated with the electric field, ionic pressure, and gravity, the horizontal divergence term of ion transport velocity is approximated as

$$\nabla_h \cdot \vec{V}_{i,h} \approx \left(\frac{\cos^2 \Theta_D}{1 + \zeta^2} \frac{k_y^2}{k_x^2 + k_y^2} + \frac{\zeta^2}{1 + \zeta^2} \right) \nabla_h \cdot \vec{V}_{n,h} \quad (17)$$

where k_x and k_y are the gravity wave horizontal wave numbers in x and y directions.

As derived in Yu [2014] for the case of gravity wave-induced neutral winds, the divergence of horizontal neutral winds can be parameterized in terms of the gravity wave-induced vertical wind and other known parameters as

$$\nabla_h \cdot \vec{V}_{n,h} = \frac{gV_{n,z} - C_s^2 \frac{\partial V_{n,z}}{\partial z}}{C_s^2 - \frac{\omega^2}{k_h^2}} \quad (18)$$

where $V_{n,z}$ is the gravity wave-induced vertical neutral wind, ω and k_h are respectively the angular frequency and horizontal wave number of the gravity wave, and $C_s = \sqrt{\gamma p_0 / \rho_0}$ is the speed of sound. Here p_0 and ρ_0 are

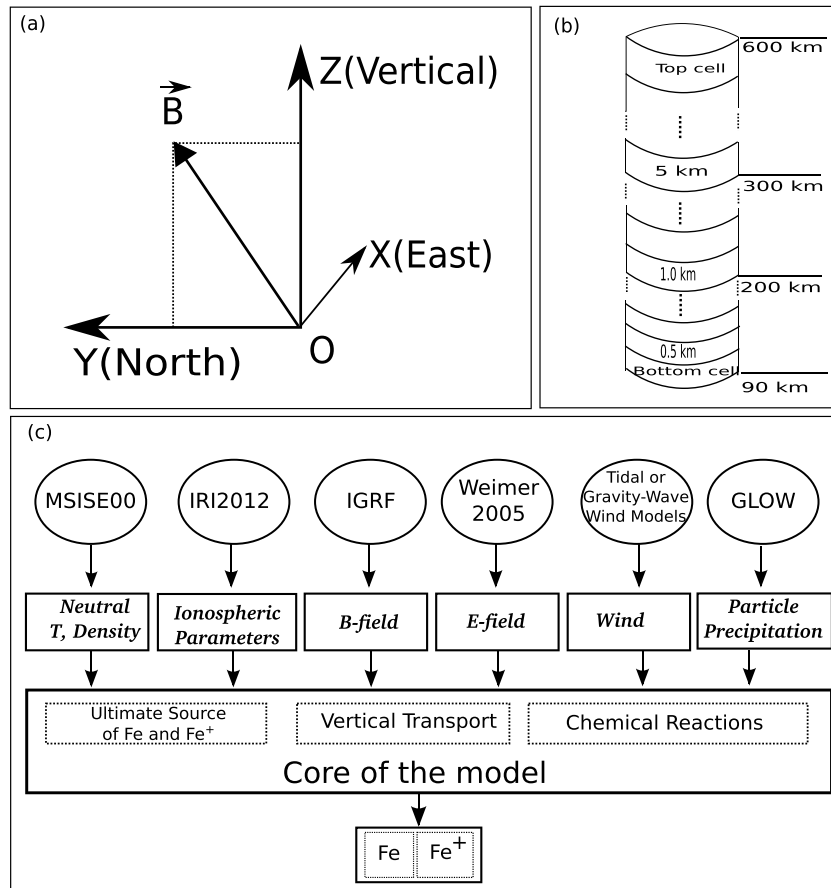


Figure 2. Schematics of the coordinate system and structure of the University of Colorado thermosphere-ionosphere Fe/Fe⁺ (TIFe) model. (a) A right-handed Cartesian coordinate system built upon the geomagnetic coordinates. (b) Finite volume cell geometry in the 1-D numerical configuration along altitude (single vertical stack). (c) The TIFe model structure includes three main modules as the core, two main outputs, and related external models used to provide necessary input parameters.

the unperturbed background atmosphere pressure and mass density, and γ is the ratio of the specific heat under constant pressure to the specific heat under constant volume. With such parameterized horizontal divergence terms given by equations (16)–(18), the 1-D TIFe model that precisely tracks the vertical winds can numerically resolve the 3-D transport term in equation (1), thus simulating the vertical transport of minor species like Fe and Fe⁺ with the effects of horizontal divergence taken into account.

2.4. Numerical Framework and New Computation Methods

The numerical TIFe model framework is built upon a right-handed Cartesian coordinate system with geomagnetic east, geomagnetic north, and vertical up as positive X , Y , and Z (Figure 2a), a common practice when dealing with geomagnetic field [e.g., Mathews, 1998; Carter and Forbes, 1999; MacDougall et al., 2000]. Note that the magnetic declination angle is $\sim 142^\circ$ at McMurdo. Taking the configuration of a vertical lidar beam, the 1-D numerical model is built along the vertical direction consisting of a stack of grids with different spacing extending from 90 to 600 km. The cell grid is set to the highest resolution of 0.5 km for 90–200 km, the range covered by lidar measurements, and then to 1 km between 200 and 300 km, and finally, to 5 km above 300 km (Figure 2b). An ideal sink is applied at the lower boundary, by which the Fe/Fe⁺ are permanently removed from the modeled regions if the mass flux is downward at the bottom boundary. A similar treatment is applied to the top boundary when the mass flux is upward.

Figure 2c illustrates the model structure. The model core consists of three main modules: ultimate source of Fe⁺ and Fe, vertical transport, and chemical reactions. Background parameters, such as the major neutral and

ionic species, geomagnetic fields, electric fields, neutral winds and temperatures, and particle precipitation, are input from external sources such as empirical or first-principle models. The main model output is the altitude profiles of Fe and Fe⁺ densities over time. The density change in each grid is mainly caused by chemical reactions and mass exchange between two adjacent grids in the vertical direction as well as horizontal divergence parameterized above. The source term is treated as two initial profiles of Fe⁺ and Fe. Consequently, the major model computation lies in the transport and chemical modules.

The continuous variables in the continuity equation (1) are discretized at the space and time grid (x_i, y_i, z_i, t_i) , and the partial differential equation (1) is solved by the finite volume method. We adapt the Strang splitting [Strang, 1968] approach to compute the solution N_M^{n+1} at time $t^{n+1} = t^n + \Delta t$ by the following sequence of steps:

$$N_M^{n+1} = \mathbb{T}(\Delta t/2)\mathbb{R}(\Delta t)\mathbb{T}(\Delta t/2)N_M^n \quad (19)$$

where \mathbb{T} and \mathbb{R} represent the discretized transport and chemical reaction operators, respectively [Khan and Liu, 1995; Fazio and Jannelli, 2009]. Here one step of transport is split into two half steps that sandwich the calculations of the chemical reaction operator.

Comparing to the work done nearly two decades ago [Carter, 1995; Carter and Forbes, 1999], significant improvements have been made in the numerical solutions of chemical reactions and in the numerical calculations of the vertical transport, taking advantage of modern computing capabilities. A major improvement in our vertical transport module is to resolve the numerical diffusion issue that is crucial for the model to deal with converged layers that can evolve to sporadic layers of high Fe⁺ concentration within 1 or 2 km. The numerical diffusion [Durran, 2010] of the low-order algorithm experienced in the models of Carter and Forbes [1999] and MacDougall et al. [2000] would lead to unrealistic conditions of wind or electric fields in order to form these converged layers. We employ the flux-corrected transport (FCT) technique [Zalesak, 1979] in the transport module to resolve the numerical diffusion issue so that the flow of ions can be modeled accurately. FCT is an algorithm originally designed for mass transportation to handle steep gradients of mass densities, as well as shock formation [Boris and Book, 1973]. It combines a high-order solution to cancel out the diffusive errors and a low-order solution limiting the antidiffusive fluxes to maintain positivity through the use of flux limiter. We use a nonclipping flux limiter proposed by [Zalesak, 1979] in our TIFe model.

To solve the nonlinear ordinary differential equations for the chemical reactions, we adopt an algorithm for large systems of differential algebraic equations (DAEs)—the DASPK (Differential Algebraic Solver Preconditioned Krylov) solver [Brown et al., 1994]. Due to the complexity of Fe/Fe⁺ and related molecule and ion chemistry with many orders of magnitude difference in reaction rates, the numerical solutions of Fe/Fe⁺ chemistry equations could be very stiff. DASPK solves the stiff DAEs via backward differentiation formula with the Krylov method [Brown et al., 1994]. It solves the nonlinear systems at each time step via Newtonian iteration. If the solutions do not converge, the DASPK solver will automatically reduce the time step by half until the solutions of chemistry equations can converge to the desired accuracy. An advantage of using such a solver is that the solutions are independent of the sequence order of chemical reactions listed in the module. More reactions can be easily added if needed.

An advantage of the fractional step method in equation (19) is that different time integration methods can be chosen for different terms [Fazio and Jannelli, 2009]. Chemical reactions are sometimes very stiff, requiring the use of implicit methods. By using the splitting technique, we can achieve higher accuracy than without splitting, because each module is solved by a higher-order accurate method. In the current study, the time step Δt in equation (19) is 30 s, so the TIFe model runs 15 s transport, then 30 s chemistry, and last 15 s transport. In the first and last 15 s, the transport module runs with a temporal resolution of 1 s, so the transport module runs 15 times for each 15 s. For the 30 s chemistry module, the chemistry module first runs with a time step of 1 s. Then the chemical solver checks whether the numerical solutions converge. If they have not converged, the chemical module will split 1 s into two 0.5 s and solve the ODEs again. This process will continue until the solutions have converged.

2.5. Model Input and Setup

We choose to input background parameters from external sources because the model is aimed for mechanism studies, rather than self-consistently modeling the thermosphere and ionosphere. Iron

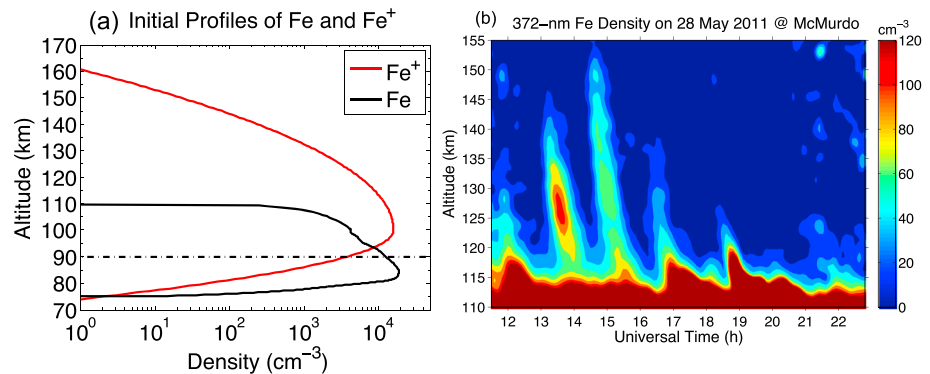


Figure 3. (a) Initial density profiles of Fe (black line) and Fe^+ (red line) used in the simulations of the thermospheric Fe layer event on 28 May 2011 at McMurdo, Antarctica. (b) Contour of thermospheric Fe densities from 110 to 155 km observed by lidar at McMurdo on 28 May 2011. Figure 3b is reproduced from *Chu et al.* [2011] for comparison to the TIFe model simulations.

species are minor constituents in the upper atmosphere; e.g., the peak number density of main Fe layers distributed between 70 and 100 km is usually 8 or more orders of magnitude less than atmospheric density [Chu et al., 2011]. Fe^+ density is usually less than 10% of electron density above 100 km [Kopp, 1997; Grebowsky and Aikin, 2002]. Therefore, the feedback of Fe and Fe^+ to the background neutral and ionized atmosphere is negligible. Only under rare circumstances, such as sporadic E layers, could Fe^+ be dominant in a thin layer because in such cases most NO^+ and O_2^+ have neutralized with converged electrons. Below we introduce the model setup.

The Fe and Fe^+ initial profiles used in our simulations of the 28 May 2011 event are shown in Figure 3a. The Fe densities below 100 km are the mean of the first half-hour lidar observations on 28 May 2011, with a peak density of $\sim 1.6 \times 10^4 \text{ cm}^{-3}$ [Chu et al., 2011]. Above 100 km, the Fe densities are set to linearly decrease to 0 at 110 km and above. Our purpose is to start the simulations with zero Fe background above 110 km and then demonstrate how the thermospheric Fe atoms are produced from Fe^+ ions that are transported into the E-F regions. The initial Fe^+ profile is set to the combination of two Gaussian profiles with a peak density of $\sim 1.6 \times 10^4 \text{ cm}^{-3}$ at 100 km. The combined Gaussians have a full width at half maximum of ~ 32.5 km above 100 km and ~ 13.9 km below it, corresponding to a total column abundance of $3.95 \times 10^{10} \text{ cm}^{-2}$. This Fe^+ initial profile is similar to the Fe^+ shown in Figure 5 of Feng et al. [2013] for WACCM-Fe over Urbana (40°N) where their peak density is $\sim 9000 \text{ cm}^{-3}$ at ~ 96 km. Given the huge variability of observed metallic ion densities [e.g., Grebowsky and Aikin, 2002; Kopp, 1997; Earle et al., 2000; Roddy et al., 2004], the Fe^+ column abundance used in our initial profile is within a reasonable range, although it is larger than some observations.

The neutral environmental data, such as neutral temperatures and number densities, are taken from NRLMSISE-00 [Picone et al., 2002], while the International Reference Ionosphere (IRI-2012) [Bilitza et al., 2011] is used to specify ionic parameters and temperatures of ions and electrons T_i and T_e . We choose to take major neutral species (N_2 , O_2 , O, H, and N) data from the NRLMSISE-00 empirical model, which are updated every 120 s. The minor neutral species (O_3 , H_2O , CO_2 , NO, and OH) data are taken from the simulation output of thermosphere-ionosphere-mesosphere electrodynamics-general circulation model (TIME-GCM) [Roble and Ridley, 1994] and updated every 120 s. The initial profiles of molecular ions (NO^+ , O_2^+ , O^+ , N_2^+ , and N^+) are set by the IRI-2012 empirical model, and these ion species densities can be updated by the TIFe model calculations, by external data every 120 s, or by the global airglow (GLOW) model [Solomon et al., 1988], which calculates ionizations under aurora and sunlit conditions. The International Geomagnetic Reference Field (IGRF-11) [Finlay et al., 2010] is used to specify the geomagnetic field (B -field) whose main field is quite stable. In contrast, the polar electric field (E -field), particle precipitation, and neutral wind fields are complex and highly variable due to the strong influences from the magnetosphere, solar activity, and wave dynamics. The empirical electric potential model of Weimer [2005] is used to set up the electric field in the TIFe model, while the GLOW model developed by Solomon et al. [1988] is utilized to characterize the ionization by auroral electron precipitation. The neutral winds in the thermosphere are the most uncertain parameters because

there are no reliable wind measurements or empirical models available, especially for the polar region under CME events. Consequently, the atmospheric (gravity or tidal) wave-induced vertical and horizontal winds along with the background horizontal winds are forward modeled in the TIFe model.

3. Fe⁺ Transport and Layering

As introduced earlier, a main question raised by *Chu et al.* [2011] is the source of Fe and Fe⁺ in the polar thermosphere and Fe⁺ layering in the polar *E* and *F* regions. Although the ultimate source of Fe and Fe⁺ is meteor input, the main meteor deposition region of Fe and Fe⁺ is below 120 km [*Vondrak et al.*, 2008]. Consequently, the background Fe⁺ density in the *E-F* region is usually low, thus insufficient to generate appreciable Fe atoms. To form neutral Fe from Fe⁺, at least two conditions are needed. First, a large amount of Fe⁺ ions must be transported from the main deposition region upward to the *E-F* regions. Second, the Fe⁺ ions in the *E-F* regions must be converged to form Fe⁺ layers that are dense enough to produce appreciable Fe atoms. These ideas are illustrated in Figure 1. The main goal of this section is to investigate the transport and convergence mechanisms. At high latitudes, previous investigations have shown that either electric field or wind shear can play important roles in transporting and converging ion layers [*Nygrén et al.*, 1984; *Bristow and Watkins*, 1991; *MacDougall et al.*, 2000]. However, it is still unknown how the wind shear mechanisms work in the presence of strong and varied electric field, especially in the polar region with high magnetic inclination angles. We utilize the method of factor separation to provide quantitative understandings of these mechanisms on transporting Fe⁺ and Fe and converging Fe⁺ layers. Both separated and combined effects of electric field, horizontal, and vertical winds are studied here.

3.1. Fe⁺ Transport by Polar Electric Field

At high latitudes, the ionospheric electric field becomes a substantial driving force of ion transport in the vertical direction [*Nygrén et al.*, 1984; *Bristow and Watkins*, 1991]. The electric field-driven vertical drift velocity V_{ize} in equation (7) can be decomposed into two components of $\vec{E} \times \vec{B}$ and \vec{E} drifts, corresponding to Hall and Pedersen drifts. We define

$$f_H = \frac{\cos\Theta_D}{1 + \zeta^2}, \quad f_P = \frac{\zeta}{1 + \zeta^2} \quad (20)$$

where f_H and f_P are the Hall and Pedersen mobility coefficients, respectively, and Figure 4a shows their altitude profiles. At high altitudes, larger Hall mobility coefficients lead to stronger $\vec{E} \times \vec{B}$ drift, while at low altitudes ions move in the direction of electric field due to larger Pedersen mobility coefficients. The directions of Hall and Pedersen drifts are determined by the electric field direction relative to the geomagnetic field line, i.e., the signs of E_x , E_y , and E_z in equation (7). Figure 4b illustrates the relationship between the electric field direction and vertical ion drift. For instance, if the electric field points to the southeast direction, both Hall and Pedersen drifts would produce upward ion flow, which suggests a potential mechanism for transporting metallic ions into the thermosphere. When the electric field points to the southwest direction, thin converged ionization layers can be formed at the null where the Hall drift moves ions downward from above and the Pedersen drift moves ions upward from below. The northeast electric field would generate an opposite effect—a divergent flow. Although the major effects are downward and upward transports, respectively, in the northwest and southeast directions of electric field, convergence can be formed under special circumstance as shown in Figure 4b. When the upper ions catch up to the lower ions in the downward flow case or when the lower ions catch up to the upper ions in the upward flow case, convergence occurs though it is not as tight as the ion convergence in the case of southwest directed electric field [*Bristow and Watkins*, 1991].

The following tests use the electric field on 28 May 2011 at McMurdo (Figure 4c) derived from the electric potential output from the Weimer-2005 empirical model [*Weimer*, 2005]. The Weimer model provides empirical high-latitude electric potentials and magnetic field-aligned currents as functions of solar wind, interplanetary magnetic field (IMF), and dipole tilt angle with greater accuracy than earlier models [*Weimer*, 2005]. The components of electric potential, which are uncorrelated to solar wind and IMF, are not included in the Weimer model. We drive the Weimer model with the hourly averaged solar wind and IMF data from <http://omniweb.gsfc.nasa.gov/>. Note that E_x , E_y , and E_z used in equation (7) are derived from the east-west and north-south electric fields ($E_{\text{East-West}}$ and $E_{\text{North-South}}$) shown in Figure 4c as follows:

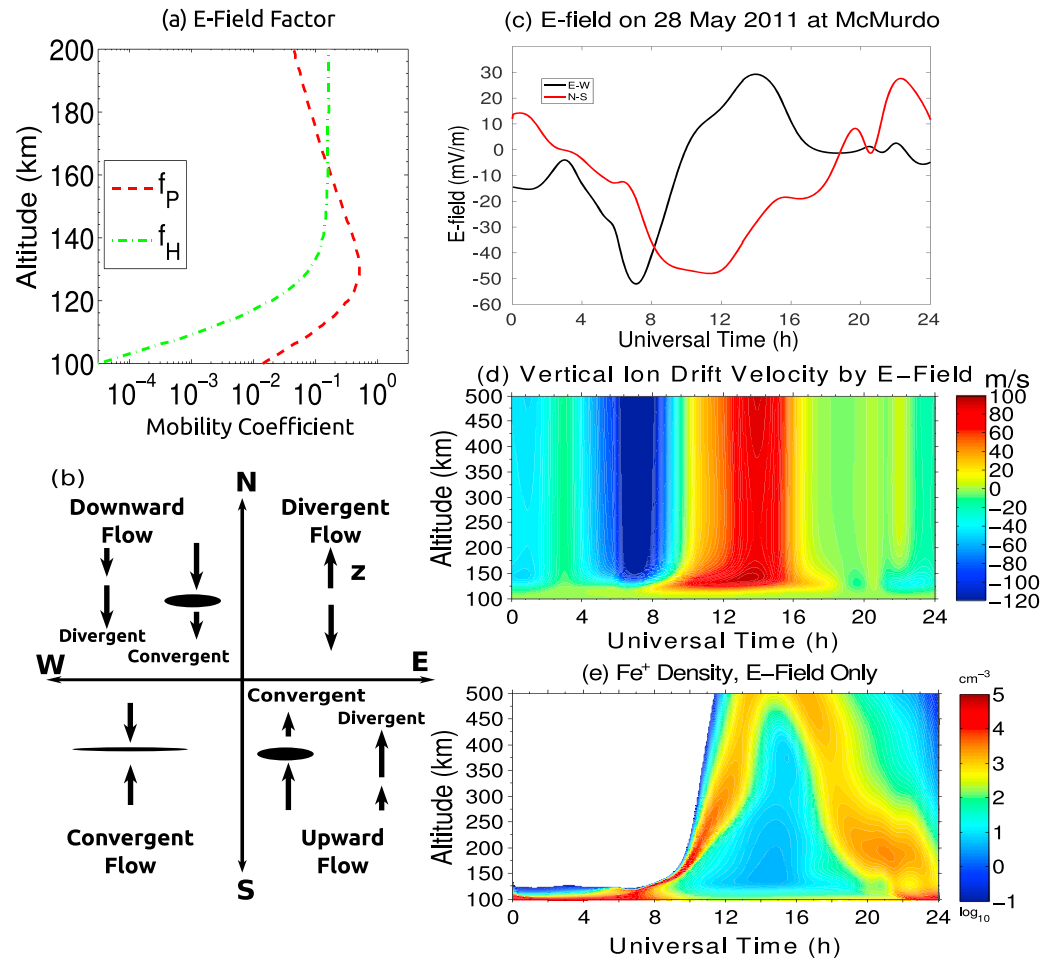


Figure 4. Fe^+ transport by polar electric field in Antarctica. (a) Comparison of Pedersen and Hall mobility coefficients. (b) Possible vertical transport of ions driven by the electric field in the Southern Hemisphere, which is inspired by Nygrén *et al.* [1984] and Bristow and Watkins [1991]. (c) The polar electric field on 28 May 2011 at McMurdo calculated from Weimer-2005 model. (d) Vertical ion drift velocity at McMurdo calculated from equation (7) using the electric field derived from Figure 4c. (e) Variations of Fe^+ densities versus time and altitude simulated with the 1-D TIFE model. Here neutral winds are turned off but the electric field, gravity, and diffusion are kept on. The chemical module and GLOW model are turned on for this simulation.

$$\begin{cases} E_x = E_{\text{East-West}} \\ E_y = E_{\text{North-South}} \cdot \sin(-\Theta_D) \\ E_z = -E_{\text{North-South}} \cdot \cos(\Theta_D) \end{cases} \quad (21)$$

The vertical drift velocity of Fe^+ (Figure 4d) is then calculated using equation (7) with the same E_x , E_y , and E_z for all altitudes (90–500 km). It is remarkable that during this CME event the polar electric field can reach ~50 mV/m strength and drive vertical ion drift to ± 100 m/s. Fast vertical ion motions up to 90 m/s between 106 and 135 km have been observed in the Arctic with incoherent scatter radars [Oyama *et al.*, 2012]. The strong electric field at high latitudes can drive substantial upward motions of Fe^+ ions, suggesting a potential mechanism of Fe^+ patches observed by Atmosphere Explorer C at altitudes around 300 km in the polar *F* region [Grebowsky and Brinton, 1978].

The variations of Fe^+ density versus time and altitude are illustrated in Figure 4e. The initial Fe^+ profile used in this simulation (Figure 3) has the majorities of Fe^+ ions distributing below 120 km. Neutral winds are turned off, but the electric field, gravity, and diffusion are kept on. From 0 to 3 UT, the electric field pointing to northwest direction moves the Fe^+ downward, thus pushing the initial layer down. From ~3 to ~9 UT when the electric field points to southwest (Figure 4c), the Hall drift pushes ions downward and the Pedersen drift

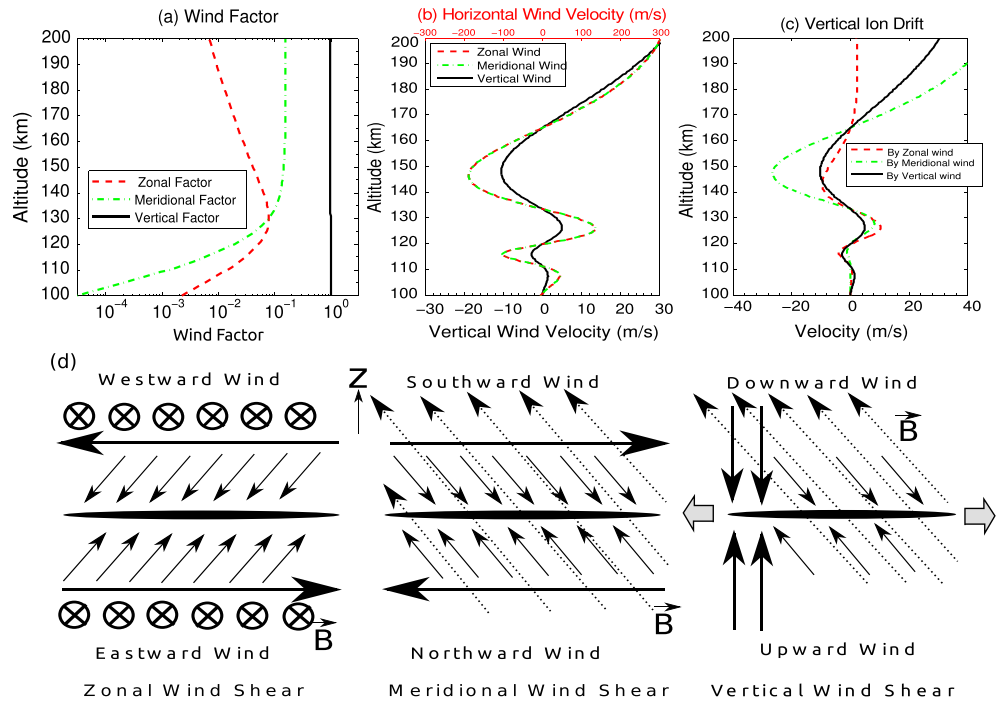


Figure 5. Fe⁺ transport by neutral winds. (a) Comparison of three wind factors by zonal, meridional, and vertical winds in producing vertical ion drift. (b) Forward modeled geomagnetic zonal, meridional, and vertical components of neutral winds induced by gravity waves at time $t = 0$, initial phase $\phi_0 = 0$, and zero background winds. (c) Vertical ion drift velocities of Fe⁺ induced by individual wind components in Figure 5b. (d) Illustration of wind shear mechanisms to converge ions by zonal (left), meridional (middle), and vertical (right) winds in the Southern Hemisphere. The grey block arrows in the right subplot indicate the horizontal divergence induced by the vertical wind shear.

pushes ions upward (Figure 4d). Consequently, the Fe⁺ ions are converged to form a thin layer around 110 km (Figure 4e). Starting from ~9 to ~16 UT, the electric field points to southeast direction so both Hall and Pedersen drifts move ions upward. Consequently, a strong upward ion flow is seen in Figure 4e, and the Fe⁺ ions in the main deposition region are transported into the F region reaching 500 km. From ~16 to ~20 UT, the east-west electric field is close to zero, while the north-south electric field is reversing its direction from south to north. During this period, the vertical ion drift is relatively slow, and the ions float at high altitudes first and then drift downward because of the gravitational force and small component of northwest electric field. Since ~20 UT the electric field starts to gain magnitudes in the northwest direction. As a result, the Fe⁺ ions are moved downward by both Hall and Pedersen drifts. Figure 4 clearly shows that the Fe⁺ ions in the main deposition region are uplifted into the F region by strong southeast directed electric field, demonstrating that the polar electric field is sufficient in transporting metallic ions into the thermosphere, thus providing the source of Fe⁺.

3.2. Fe⁺ Transport by Neutral Winds

The ionization layers can be transported or converged by vertical ion drift driven by neutral winds blowing across the geomagnetic field via Lorentz force. Equation (8) gives the vertical drift velocity V_{izw} due to neutral winds. We define the dimensionless wind factors

$$f_x = \frac{\zeta \cos\Theta_D}{1 + \zeta^2}, \quad f_y = -\frac{\sin(2\Theta_D)}{2(1 + \zeta^2)}, \quad f_z = 1 - \frac{\cos^2\Theta_D}{1 + \zeta^2} \quad (22)$$

where $f_i =_{x,y,z}$ denote the wind factors associated with the geomagnetic zonal, meridional, and vertical components of neutral winds, respectively. Three wind factors are compared in Figure 5a for McMurdo. Comparing f_x with f_y , zonal wind is more efficient at drifting ions vertically below 120 km because of the strong ion-neutral coupling, but above 130 km the meridional wind factor exceeds the zonal wind factor because less ion-neutral coupling allows ions to drift along the geomagnetic field lines. As recognized

since *Whitehead* [1961] and *Axford* [1963], the mechanisms of vertical shear of horizontal winds dominate over the vertical shear of vertical wind at the middle and low latitudes [*Carter and Forbes*, 1999; *Bishop and Earle*, 2003]. However, in the polar region the shears of horizontal winds are no longer dominant because the horizontal wind factors f_x and f_y drop fast as the geomagnetic dip angle Θ_D approaching -90° , while the vertical wind factor f_z approaches unity (Figure 5a). This situation gives rise to a much more efficient converging force by the vertical wind than by the horizontal winds. Consequently, the neutral vertical wind can induce vertical ion drift velocities with magnitudes similar to those by the neutral horizontal winds, despite the vertical wind being much smaller than the horizontal winds. We demonstrate this point in Figures 5b and 5c as the following.

To test the neutral wind mechanisms, the gravity-wave-induced neutral winds are forward modeled using the observed gravity wave parameters [*Chu et al.*, 2011]. The gravity wave on 28 May 2011 shows a period of ~ 1.5 h between 75 and 155 km, and the vertical wavelength changes from ~ 15 km at 100 km to ~ 70 km at 150 km [*Chu et al.*, 2011]. We assume a monochromatic gravity wave with a period of 1.57 h. Its vertical wavelength is set up by the lidar observations below 155 km and approximated by the vertical wavelength profiles in *Vadas* [2007] above 155 km. The horizontal wavelength is estimated by comparing the measured vertical wavelengths with the calculated vertical wavelengths in *Vadas* [2007] and *Djuth et al.* [2010], giving rise to the best estimation of ~ 800 km. As the horizontal wavelength remains constant with altitude if the background winds and temperatures change only with altitude [*Vadas and Nicolls*, 2009], the horizontal wavelength is set to a constant 800 km throughout the altitude range in the model. The horizontal wave number is $k_h = \sqrt{k_x^2 + k_y^2}$, and the vertical wave number is $m < 0$ for downward phase progression [*Fritts and Alexander*, 2003]. We set k_x to positive and $k_x = k_y$, meaning that the gravity wave propagates in the geomagnetic northeast direction. The wave-induced vertical (w) and horizontal (u_h) winds at 150 km are modeled as

$$\begin{cases} w(t, x, y, z_0) = w(z_0) \cos(\omega t - k_x x - k_y y - m z + \phi_0) \\ u_h(t, x, y, z_0) = -\frac{m}{k_h} w(z_0) \cos(\omega t - k_x x - k_y y - m z + \phi_0) \end{cases} \quad (23)$$

Here a simplified polarization relationship is applied [*Fritts and Alexander*, 2003]:

$$u_h = -\frac{m}{k_h} w. \quad (24)$$

Note that an initial phase ϕ_0 is introduced for adjusting the phase relation between the neutral winds and electric field in the model. We assume that the vertical wind amplitude at $z_0 = 150$ km is $w(z_0) = \sim 12$ m/s. Below 200 km the amplitude is calculated as $w(z) = w(z_0) \sqrt{\rho(z_0)/\rho(z)}$, where ρ is the atmosphere density [*MacDougall et al.*, 2000], and above 200 km $w(z > 200 \text{ km}) = w(z = 200 \text{ km})$. Such forward-modeled vertical winds are comparable to the vertical winds reported by *Larsen and Meriwether* [2012]. The modeled wind profiles are shown in Figure 5b for time $t = 0$, $\phi_0 = 0$, and zero background winds.

Using the modeled neutral winds (Figure 5b), we compute the vertical drift velocities of Fe^+ caused by each wind component. The results are compared in Figure 5c. Below 110 km, the vertical drifts caused by horizontal winds are close to zero, and Fe^+ ions follow the neutral vertical wind and converge at the null of vertical wind. Above 120 km, the vertical drift caused by meridional wind increases fast with increasing altitude, since f_y and meridional wind amplitude increase at the same time. The vertical drift caused by zonal wind increases fast around 120 km due to increasing f_x and zonal wind amplitude but then decreases with increasing altitude as the increase of zonal wind amplitude is canceled out by the decrease of f_x . Because the background horizontal winds are not considered, the nulls of zonal, meridional, and vertical winds coincide, making the nulls of vertical ion drifts by three winds identical at the same altitudes. Once the background winds are considered, the nulls caused by the horizontal winds can deviate from those by the vertical wind. The local maximum of the vertical drift is determined by the product of wind factor and wind amplitude; therefore, the altitudes of the local maxima of three vertical ion drifts can be different from each other, even when the background winds are assumed zero. Figure 5d illustrates the ion transport and convergence mechanisms by the (geomagnetic) zonal, meridional, and vertical winds in the polar region.

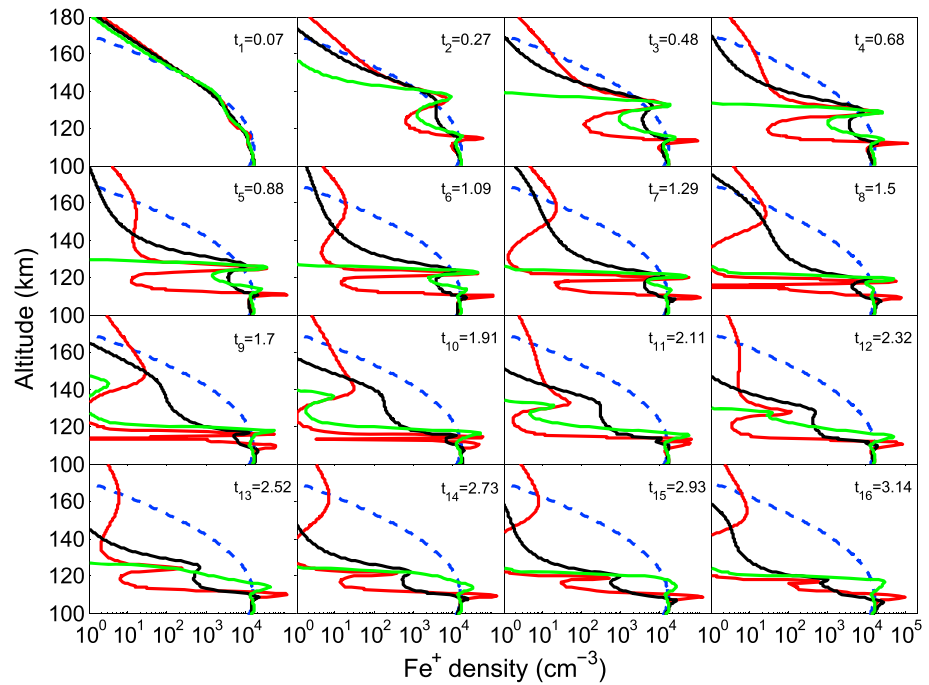


Figure 6. Experiments to test the impacts of neutral wind shear mechanisms on the transport and convergence of polar Fe^+ ions. The electric field is turned off, but one of the three wind components is switched on each time at $t = 0$. The chemistry module is first run for 0.6 h but then turned off once the transport module is turned on at $t = 0$. The horizontal divergence associated with the vertical wind is included, and gravity and diffusion are also included. The blue dashed line indicates the initial Fe^+ density profile used in the experiments, while the red, green, and black solid lines represent the Fe^+ density profiles converged only by the zonal, meridional, or vertical winds, respectively. The simulation time is indicated by the number on the top right corner of each subplot in the unit of hour.

To investigate the impacts of neutral wind shear mechanisms on the transport and convergence of polar Fe^+ ions, we design an experiment in Figure 6, in which the electric field is turned off but one of the three neutral winds in geomagnetic coordinates (shown in Figure 5b) is switched on each time at time $t = 0$ with an initial phase $\phi_0 = 0.2\pi$. Each simulation starts with the chemistry module only for 0.6 h before $t = 0$ to allow the system to reach chemical balance. Once the transport module is turned on, the chemistry module is turned off; thus, any changes of Fe^+ densities since $t = 0$ are induced only by the wind transport. The initial profile of Fe^+ is given by the blue dashed line in Figure 6, whose Fe^+ densities at higher altitudes are substantially higher than those of the initial profile shown in Figure 3. We compare the evolutions of the Fe^+ profiles with three distinct wind inputs: zonal, meridional, and vertical winds only. The rest initial conditions for McMurdo are identical for these three simulations. Figure 6 shows that all three winds can transport Fe^+ both upward and downward, since the wave-induced winds reverse directions periodically, but, in general, the simulations give downward transport of Fe^+ . The upward transport of Fe^+ can be seen at the beginning of the simulation when Fe^+ densities exceed the initial profile density above 170 km. The occurrence of a peak at ~ 140 km around 1.7 UT is also an evidence of upward transport of Fe^+ by the meridional wind. Because the gravity wave-induced neutral wind amplitudes grow with altitude, the wind amplitudes used in the simulation (Figure 5b) are much larger at higher altitudes than at lower altitudes. Consequently, it is efficient for the winds to push Fe^+ downward from higher altitudes but much less efficient to push Fe^+ upward from lower altitudes. Such wave-induced wind profiles lead to the overall downward trend of Fe^+ transport by neutral winds.

All three winds are effective in forming vertically converged Fe^+ layers as shown in Figure 6. Although the vertical wind factor f_z is the largest among f_x , f_y , and f_z (Figure 5a), the vertical wind amplitudes are much smaller than those of zonal and meridional winds (Figure 5b) for the gravity wave observed by the lidar. As a result, the overall convergence effects by the vertical wind are somewhat comparable to or weaker than those by the horizontal winds in Figure 6. The meridional wind is highly effective in converging Fe^+ at

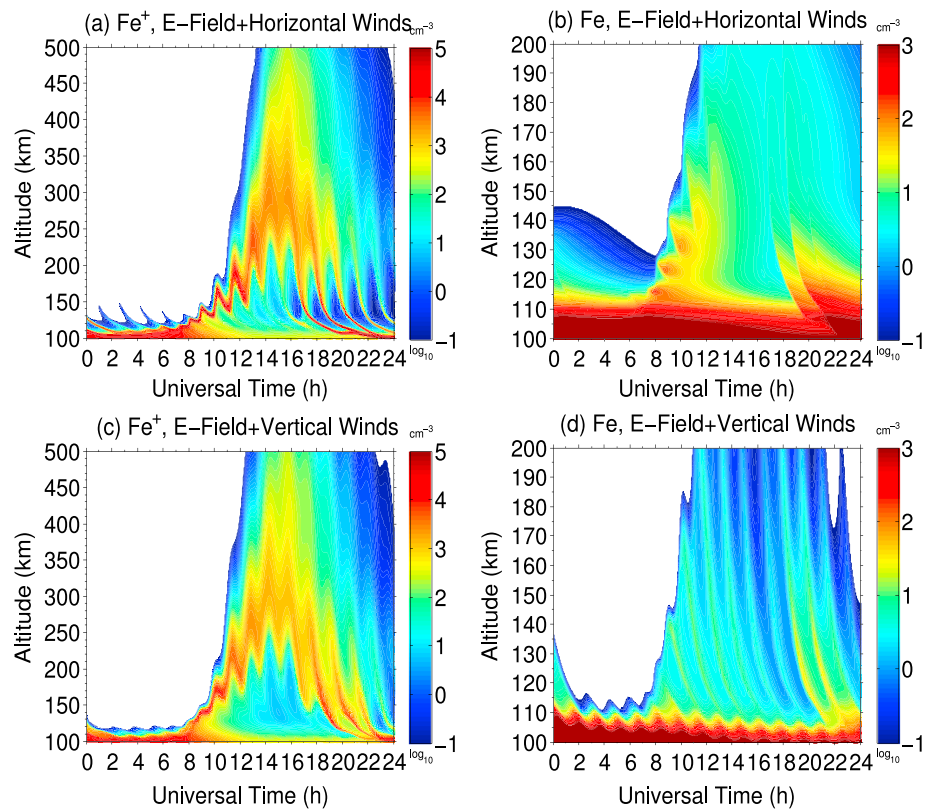


Figure 7. Fe^+ and Fe transport in the simultaneous presence of polar electric field and neutral winds. (a and b) Fe^+ and Fe density variations under the electric field and horizontal winds. The vertical wind is turned off. (c and d) Fe^+ and Fe density variations under the electric field and vertical winds. The horizontal divergence is included in the simulation, but the horizontal winds are turned off. The chemical module and GLOW model are turned on for all four subplots.

high altitudes, while the zonal wind is effective at lower altitudes. The altitudes of Fe^+ layer peaks are separated from the present wind nulls because the formation of Fe^+ layer peaks is related to the previous convergent nulls. When the convergent nulls move downward as the gravity wave propagating upward, the converged Fe^+ layers are not able to follow the wind nulls, so the present wind null is below the peak of Fe^+ layer. When the divergent nulls catch up the converged Fe^+ layers, the Fe^+ layers would be broadened by the divergent wind. The experiment in Figure 6 demonstrates that the neutral wind shear mechanisms can still transport and converge ion layers in the polar region with high magnetic inclination angles as long as the wind shears are sufficient. The wind amplitudes (Figure 5b) used in the simulations are in the reasonable range of observed neutral winds in the thermosphere. The horizontal and vertical wind shears can have comparable effects on ion transport and convergence, depending on altitudes and relative wind magnitudes.

3.3. Fe^+ and Fe Transport in the Simultaneous Presence of Electric Field and Winds

The motions of Fe^+ are governed by both electric field and neutral winds. The convection electric field has more profound impact on the vertical redistribution of Fe^+ at high latitudes than at low latitudes. In Figure 7, we investigate how the wind mechanisms work in the presence of polar electric field. The simulation conditions for Figure 7 are identical to those for Figure 4e except now the neutral winds given by Figure 5b are turned on since the beginning. Horizontal winds are applied to Figures 7a and 7b, while vertical wind is applied to Figures 7c and 7d. Despite some small differences, the overall patterns of Fe^+ motion over the 24 h time span are similar between Figures 7a and 7c, which are determined by the diurnal variations of electric field and the periodic variations of neutral winds induced by gravity waves. The electric field first pushes Fe^+ downward, then reverses its direction to uplift Fe^+ to several hundreds of kilometers, and then reverses again to transport Fe^+ downward, showing the overall Fe^+ envelope similar to Figure 4e. In contrast to the

“smooth” Fe^+ densities in Figure 4e, periodic multiple Fe^+ layers are seen from 0 to 8 UT in Figure 7a, periodic “up and down” oscillations of Fe^+ layers are seen from 8 to 16 UT in Figures 7a and 7c, and periodically converged Fe^+ layers are seen from 16 to 24 UT in Figures 7a and 7c. Such periodic behaviors with a time scale of 1–2 h are certainly caused by the gravity-wave-induced neutral winds. The results in Figure 7 demonstrate that neutral winds can still converge Fe^+ layers in the presence of electric field.

Although neutral winds can transport Fe^+ upward efficiently at higher altitudes as demonstrated in Figure 6, the major upward transport of Fe^+ in Figure 7 is driven by the electric field because the neutral winds used in this study have small amplitudes at lower altitudes, thus less efficient than the polar electric field in transporting Fe^+ upward from the main deposition region. This fact explains why the upward phase progression of Fe^+ layers only shows up clearly from 8 to 16 UT when the electric field is in the southeast direction for upward transport, but such upward phase does not show up or is less clear from 0 to 7 UT and from 17 to 24 UT when the electric field is not in the direction of uplifting Fe^+ . Though multiple converged Fe^+ layers are formed with downward phase progression at these two time durations, they are converged from the remaining Fe^+ ions that have not been transported downward yet. With the vertical and horizontal wind amplitudes used in this study, the horizontal winds converge Fe^+ more strongly than the vertical wind, as the converged Fe^+ layers in Figure 7a have higher densities than the corresponding layers in Figure 7c, supporting the results of Figure 6. The electric field can have constructive or destructive effects with the neutral winds in converging Fe^+ layers, depending on their phase relation. As an example, the strong thin Fe^+ layers are formed via the constructive effects of downward transport of electric field with wind shears from 17 to 24 UT in Figure 7a.

While they have comparable effects on converging Fe^+ ions, the horizontal and vertical winds have very different effects on transporting the neutral Fe atoms as demonstrated in Figures 7b and 7d. Broad thermospheric Fe layers are found in Figure 7b when there is no vertical wind. Under this circumstance, the Fe atoms are localized and lost only through charge transfer and ionization if horizontal homogeneity in Fe density is assumed. Since the lifetime of Fe atoms is much longer than the wave period, the second Fe layer emerges when the first Fe layer has not been depleted. In contrast, when the vertical wind is present in Figure 7d, the produced Fe layers become much narrower in time span than those in Figure 7b. In this case, the neutral Fe atoms are transported downward by the vertical wind following the phase of gravity wave. Because the Fe layer shape in Figure 7d is much closer to the lidar observations (Figure 3b) than that in Figure 7b, it demonstrates the importance of vertical wind in shaping the observed Fe layers. It is worth pointing out that the Fe^+ layers in the downward phase have much higher densities than those in the upward phase during the Fe^+ “oscillations” from 8 to 16 UT, leading to more production of neutral Fe in the downward phase than in the upward phase. Moreover, the upward phase of Fe^+ is associated with the divergent nulls of the neutral winds, which will further decrease the neutral Fe densities in the upward phase. The convergent nulls of the neutral winds associated with the downward phase of Fe^+ help converge the produced Fe together to form Fe layers detectable by lidar. Therefore, Figures 7b and 7d exhibit appreciable neutral Fe densities in the downward phase and nearly negligible Fe in the upward phase.

4. Fe^+ Neutralization via Fe and Fe^+ Chemistry

What major mechanisms are responsible for converting Fe^+ to Fe is another main question raised by *Chu et al.* [2011]. Basically, there are two known channels of neutralizing Fe^+ to form Fe atoms. The first channel is direct electron- Fe^+ recombination. That is, Fe^+ ions directly combine with electrons to produce Fe atoms via radiative recombination (RR) and dielectronic recombination (DR) [Nahar et al., 1997]. Both RR and DR lead to emission of a photon with energy $h\nu \geq 7.9$ eV (R1):

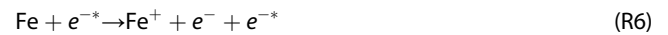


Such direct recombination reactions are slow, and the total recombination rate coefficients are around 6.5×10^{-12} and 5.2×10^{-12} $\text{cm}^3 \text{s}^{-1}$ at temperatures of 300 and 500 K, respectively [Nahar et al., 1997]. The second channel is dissociative electron recombination. That is, once Fe^+ is oxidized by O_3 to produce more active FeO^+ (R2), an electron will react with FeO^+ to dissociate the molecule and form a neutral Fe atom in the meantime (R3).



However, FeO^+ is also quite reactive with atomic O that converts FeO^+ back to Fe^+ (R4). The competition between R3 and R4 leads to a lifetime of Fe^+ that highly depends on the density ratio of atomic O and O_3 in the upper mesosphere and lower thermosphere [Plane, 2003]. Because its reaction rate coefficient is on the order of $10^{-7} \text{ cm}^3 \text{ s}^{-1}$ [Plane *et al.*, 1999], the dissociative recombination reaction (R3) is significantly faster than R1. However, above 115 km, O_3 is significantly reduced because the extremely low pressure prevents the formation of O_3 from the recombination of O and O_2 [Allen *et al.*, 1984; Plane, 2003], and photolysis consumes O_3 efficiently. Consequently, it is expected that FeO^+ concentration above 115 km is insufficient for producing the observed Fe density via R3 and R4 competition, so the neutralization of Fe^+ above 115 km is mainly through direct recombination R1 as hypothesized in Chu *et al.* [2011].

Such a theory must be tested with quantitative simulations. Furthermore, whether the direct electron- Fe^+ recombination (R1) is sufficient to produce the lidar-observed Fe density requires detailed quantitative modeling investigations. This is because the slow production reaction must compete with various loss reactions that convert Fe back to Fe^+ or to compound molecules. Once neutral Fe is formed, it can be lost through photoionization (R5), ionization caused by energetic electrons (R6), charge transfer reactions with O_2^+ and NO^+ (R7 and R8), and oxidization by O_3 (R9):



The loss of Fe is mainly through charge transfer and photoionization if there is sunlight above 115 km where O_3 is lacking. Under dark polar night conditions, photoionization is absent but aurora particle precipitation may have significant impacts on the production and loss of Fe via increasing NO^+ , O_2^+ , and electron densities and ionizing Fe by direct impact (R6). The major goal of this section is to investigate the chemical production and loss mechanisms of Fe, test the theory of Chu *et al.* [2011], and inspect the roles of aurora activity.

4.1. Tests of Fe^+ Neutralization Mechanisms

To test the hypothesis of direct recombination being the major channel to convert Fe^+ to Fe in the thermosphere as proposed by Chu *et al.* [2011], the following two model runs are performed. In the first run, we shut down the direct electron- Fe^+ recombination (R1) by setting the reaction rate coefficient $k_1 = 0$ while keeping all other coefficients in Tables 1 and 2. In the second run, we shut down the dissociative recombination (R3) by setting $k_3 = 0$ while keeping all other coefficients including k_1 in Tables 1 and 2. The model conditions of source and transport are kept the same for both runs, in which the electric field is 45% of that given by Figure 4c, the horizontal and vertical winds are given by Figure 5b, the initial Fe and Fe^+ profiles are given in Figure 3, and the horizontal wind divergence is turned off. All initial parameters of major and minor species of neutrals and ions are kept the same for both runs. The simulations start at 11 UT with only chemistry for the first half hour and then run with chemistry and transport modules thereafter. The results of these two runs are compared in Figure 8, and the differences are stunning. Above ~ 125 km, the dissociative recombination is ineffective to produce Fe atoms because of the low O_3 concentration (Figure 8a). Although the direct recombination is slow, it is sufficient to produce appreciable Fe densities above 120 km as shown in Figure 8b. Below 120 km, the situation is reversed; i.e., the first run with (R3) generates significantly more Fe densities than those by the second run with (R1). Certainly, to what altitudes (R3) is effective depends on the O_3 concentration profile as well as on how effective the competing reaction (R4) is. Nevertheless, Figure 8 demonstrates clearly that the major neutralization mechanism above ~ 120 km is the direct recombination (R1), supporting the hypothesis made by Chu *et al.* [2011].

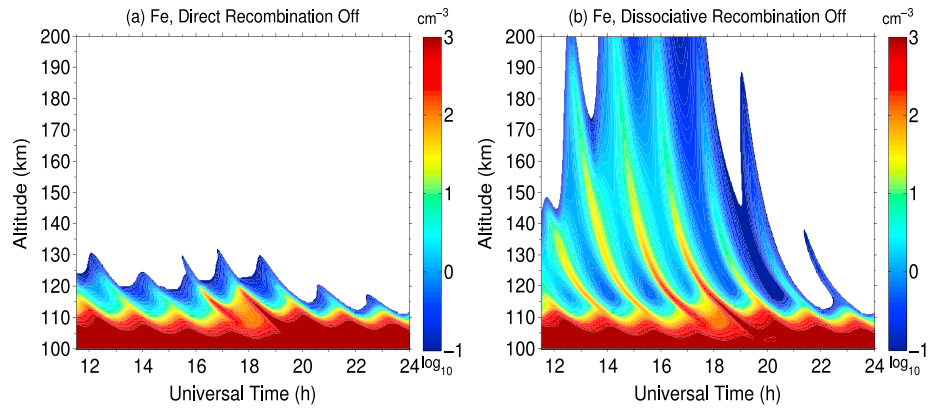


Figure 8. Tests of Fe⁺ neutralization channels in the thermosphere. Fe density contours produced by two TIFE model runs with (a) the direct electron-Fe⁺ recombination channel shut off and (b) the dissociate recombination channel shut off, respectively. In these two simulations, the GLOW model is turned on with energy influx of 1.5 erg/s/cm², but the horizontal divergence is turned off. The electric field is reduced to 45% of the original strengths calculated from Weimer model.

Why is the slow reaction R1 able to produce appreciable Fe densities? We investigate it by comparing the production and loss rates of Fe. The production rate of Fe via (R1) as a function of Fe⁺ and electron densities is shown in Figure 9a, while the loss rate of Fe by charge transfer as a function of NO⁺ and O₂⁺ densities is given in Figure 9b. The production rate is on the order of 0.085 cm⁻³ s⁻¹ for [e⁻] = 1.5 × 10⁵ cm⁻³ and [Fe⁺] = 1.0 × 10⁵ cm⁻³ at 400 K, while the charge transfer loss rate is on the order of 0.02 cm⁻³ s⁻¹ for [NO⁺ + O₂⁺] = ~5 × 10⁴ cm⁻³ and Fe density of 400 cm⁻³. Because the thermospheric Fe layers were observed during dark polar nights, photoionization of Fe is absent. The low concentration of O₃ makes the loss of Fe and Fe⁺ through oxidization negligible. If the Fe ionization by direct impact of aurora energetic particles is also small, the production and loss rates shown in Figure 9 are the major ones for Fe, while the production of Fe via (R1) is the major loss mechanism for Fe⁺. Using these rates, we estimate in the thermosphere that the Fe⁺ lifetime is on the order of 10 days, and the Fe lifetime varies from several hours to about a day depending on the concentrations of NO⁺ and O₂⁺, when the downward transport of Fe⁺ and Fe by gravitational force is neglected. It is clear from these simulations that a very small portion (on the order of ~0.1%) of Fe⁺ is converted to Fe via (R1). Because the converged Fe⁺ layers possess high densities (on the order of 10⁵ cm⁻³) and the Fe loss rate in dark night is low, ~0.1% conversion rate is sufficient to produce the observed Fe densities via R1.

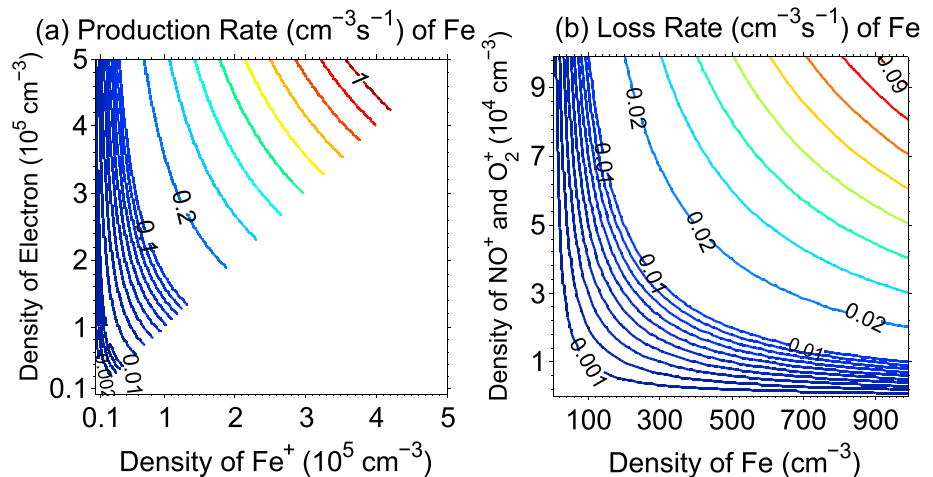


Figure 9. Production and loss rates of Fe in the thermosphere. (a) The production rate of Fe via the direct recombination reaction (R1) under different electron and Fe⁺ densities. (b) The loss rate of Fe via charge transfer with NO⁺ and O₂⁺.

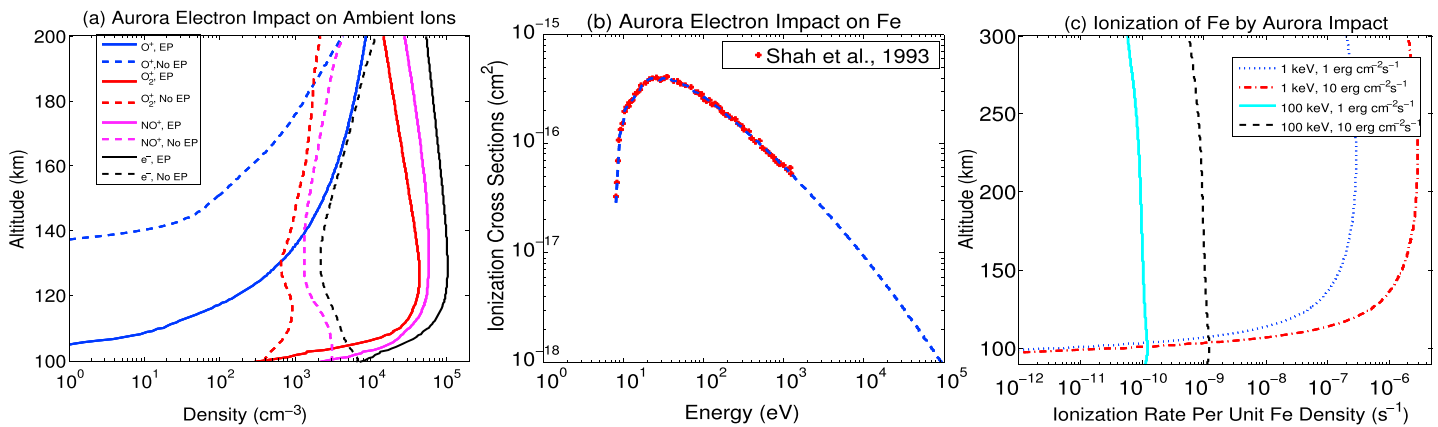


Figure 10. (a) Plasma density profiles (solid lines) given by the GLOW model under aurora precipitation on 28 May 2011, compared with the plasma densities (dashed line) taken from the IRI model for the nighttime conditions. (b) Ionization cross section of Fe by aurora electron impact obtained via extrapolation of the experimental data in *Shah et al.* [1993]. (c) Profiles of ionization rates of Fe by aurora electron impact per unit Fe density for different values of electron energy spectrum and energy influx.

4.2. Impacts of Aurora Activity

Aurora electron precipitation has substantial effects on the partitioning chemistry between Fe and Fe⁺, because energetic electron precipitation penetrating into the thermosphere and mesosphere can cause significant changes of chemical constituents [*Aikin and Smith, 1999; Sinnhuber et al., 2012*] and ionization of neutral atmosphere [*Frahm et al., 1997*]. The thermospheric Fe layer events reported in *Chu et al.* [2011] were observed during diffuse aurora activity, so it is worthwhile to investigate how aurora impacts the formation of Fe layers. In contrast to the discrete aurora that has sharply peaked spectrum, diffusive aurora has continuous temporal and large extent spatial signature [*Lui et al., 1973*]. Diffusive aurora typically comprises the major energy of aurora input into the polar upper atmosphere [*Sandford, 1968*] and has uniform impacts on the *E-F* region over spatial scale of thousands of kilometers and time scale of hours [*Whalen, 1983; Robinson and Vondrak, 1985*]. Aurora electrons can increase plasma density by enhancing the ionization of neutrals, as parameterized by various methods [*Roble and Ridley, 1987; Solomon et al., 1988; Solomon, 2001; Fang et al., 2008*]. The increased electron density can speed up the neutralization of Fe⁺ to form Fe (R1), while increased NO⁺ and O₂⁺ densities can increase Fe⁺ density and the loss of Fe through enhanced charge transfer (R7 and R8). Aurora can reduce O₃ concentration in the upper mesosphere and thermosphere by increasing readily oxidizable substances like NO_x and OH [*Sinnhuber et al., 2012*]. The energetic electrons generated by aurora can also ionize Fe through direct impact.

The GLOW model is adopted in our model to compute the energetic electron flux introduced by aurora electron precipitations. The GLOW model is an energetic electron transport and energy deposition model, providing ionization and excitation rates of major species, energetic electron production and transport, excited species densities, and airglow emission rates for the thermosphere [*Solomon et al., 1988; Bailey et al., 2002*]. Typically, the energy spectrum of diffusive aurora electrons is from 0.1 eV to ~50 keV with Maxwellian energy distribution with a mean energy of tens of eV. The energies of major aurora electrons are well above the thresholds of ionization energy of atmosphere gases (on the order of tens eV), creating energetic secondary electrons during the process of auroral electrons ionizing neutral gases. The roles of primary and secondary electrons in all radiation and ionization phenomena have been recognized for decades [*Green and Sawada, 1972; Solomon et al., 1988*]. The GLOW model utilizes the two-stream formalism of *Nagy and Banks* [1970] to calculate the primary and secondary electron fluxes, as well as the photoelectron flux generated by solar irradiance. The solid lines in Figure 10a are the average electron and molecular densities over the 12 h modeling with auroral electron precipitation on 28 May 2011, and the dashed lines are the plasma densities taken from the output of IRI model for nighttime conditions. The comparison shows that the electron densities are enhanced by 2 orders of magnitude and so are the densities of NO⁺, O₂⁺, and O⁺.

The ionization rate of Fe by direct electron impact is not given in the GLOW model. We utilize the ionization cross sections of Fe measured in the laboratory by *Shah et al.* [1993] to quantify the ionization rate of Fe by energetic electrons. The cross section of R6 was measured for the electron energy spectrum from an

ionization threshold of 8 eV to 1.25 keV [Shah *et al.*, 1993]. We fit an exponential function, $\sigma_{\text{Fe}}(E > 100 \text{ eV}) = e^{aE^2 + bE + c}$, to the measured values between 100 and 1250 eV and then extrapolate to obtain the ionization cross sections above 1.25 keV. By minimizing the fitting error, we obtain that $a = -0.0398$, $b = -0.181$, and $c = -34.169$. Below 100 eV, the cross section at any electron energy is interpolated from the measured values. The resulted ionization cross section used in our model is shown as the blue line in Figure 10b. The ionization rate of Fe, $I_{\text{Fe}}(z)$, is then calculated as a function of the total electron flux per unit energy $\phi(E, z)$, ionization cross section $\sigma_{\text{Fe}}(E)$, and number density of Fe $n_{\text{Fe}}(z)$ as

$$I_{\text{Fe}}(z) = \int_{E_T}^{\infty} \phi(E, z) \cdot \sigma_{\text{Fe}}(E) \cdot n_{\text{Fe}}(z) dE, \quad (25)$$

where E_T is the threshold of ionization energy of Fe. Note that $\phi(E, z)$ includes all electrons of primary and secondary electrons as well as photoelectrons. The calculated ionization rates per unit Fe density (in unit of s^{-1}) of Fe are plotted against altitude in Figure 10c for four conditions of auroral electron input. The energetic electron flux produced by auroral electron precipitations is determined by both total input energy flux and electron energy spectrum. Figure 10c shows that larger total energy influx generates more energetic electrons, leading to the higher ionization rate than that with less energy influx but the same energy spectrum. Under the same total input energy flux, the 100 keV auroral electrons have lower altitude of peak electron flux than 1 keV electrons, leading to less ionization at the upper altitudes but more ionization at the lower altitudes [Fang *et al.*, 2008]. It is clear from Figure 10c that the ionization rate of unit Fe density is around 10^{-6} s^{-1} or less, so the loss rate of Fe caused by direct ionization by aurora energetic electrons is significantly smaller than the loss rate caused by charge transfer.

Auroral electron precipitation plays the role of a double-edged sword in the formation of thermospheric Fe layers. On one hand, the energetic electron fluxes created by auroral electrons significantly enhance the electron densities in the E - F regions, accelerating the production of Fe via neutralization of Fe^+ . On the other hand, aurora increases the loss of Fe via enhanced charge transfer with increased densities of NO^+ , O_2^+ , and O^+ and via electron impact ionization. The competition of production and loss of neutral Fe is determined by plasma densities for a given Fe^+ abundance. Figure 11 illustrates an experiment designed to investigate the impact of aurora. The test uses square-shaped initial Fe^+ and Fe profiles, in which Fe^+ ions of 10^4 cm^{-3} distribute from 150 to 160 km and Fe atoms of 200 cm^{-3} distribute from 120 to 130 km. The electric field is set to 1 mV/m, pointing to the east. Uplifted by the electric field, the Fe^+ layer shows an upward motion (Figures 11a and 11c). The neutral winds are set to zero, so only gravity and diffusion impact the motion of neutral Fe. When GLOW is on, the Fe layer in Figure 11b is depleted via charge transfer with NO^+ and O_2^+ while Fe^+ ions are produced around 120 km. The Fe layer exhibits a slow downward motion caused by gravity. In the region with initial Fe^+ but zero Fe, say 160 km, there is no neutral Fe in the beginning but then Fe atoms are produced through neutralization of Fe^+ . Since the Fe^+ density is high in the beginning, the net gain of Fe atoms is seen at first. Then after 15.5 UT, the major Fe^+ ions are moved away from 160 km by electric field, so Fe^+ and Fe layers are decoupled and a net loss from Fe layer is seen at 160 km. At higher altitudes, the Fe densities are increased due to the increasing densities of Fe^+ . When GLOW is off, fewer Fe^+ ions are produced around 120 km via charge transfer of the initial Fe layer with lower NO^+ and O_2^+ densities. Above 140 km, it is hard to see net Fe production from Fe^+ neutralization because of the lower electron density. A diffusive Fe layer originated from the initial Fe layer is formed by diffusion. Because of the shape of the initial Fe layer, the large density gradient on the top edge of Fe layer gives rise to very large diffusion velocity (see equation (12)). This test demonstrates that energetic electron precipitation from diffusive aurora enhances neutralization of Fe^+ in converged Fe^+ layer by increasing the electron densities. When Fe and Fe^+ layers are decoupled, the lack of Fe production leads to a net loss of Fe via charge transfer with NO^+ and O_2^+ . This net loss of Fe can be enhanced by an increase in NO^+ and O_2^+ densities due to aurora particle precipitation.

5. Simulations of Fe Layer Event on 28 May 2011 at McMurdo

Even after examining the mechanisms of Fe^+ and Fe transport and chemistry, there are still questions about what determines the observed Fe layer shapes and why the event on 28 May 2011 follows gravity wave phases so precisely. Multiple factors, such as the polar electric and geomagnetic fields, neutral vertical and horizontal winds, initial Fe^+ layer conditions (external sources), atmospheric waves, and aurora particle precipitation, are expected to play roles. In addition to the effects of individual factors, the relative

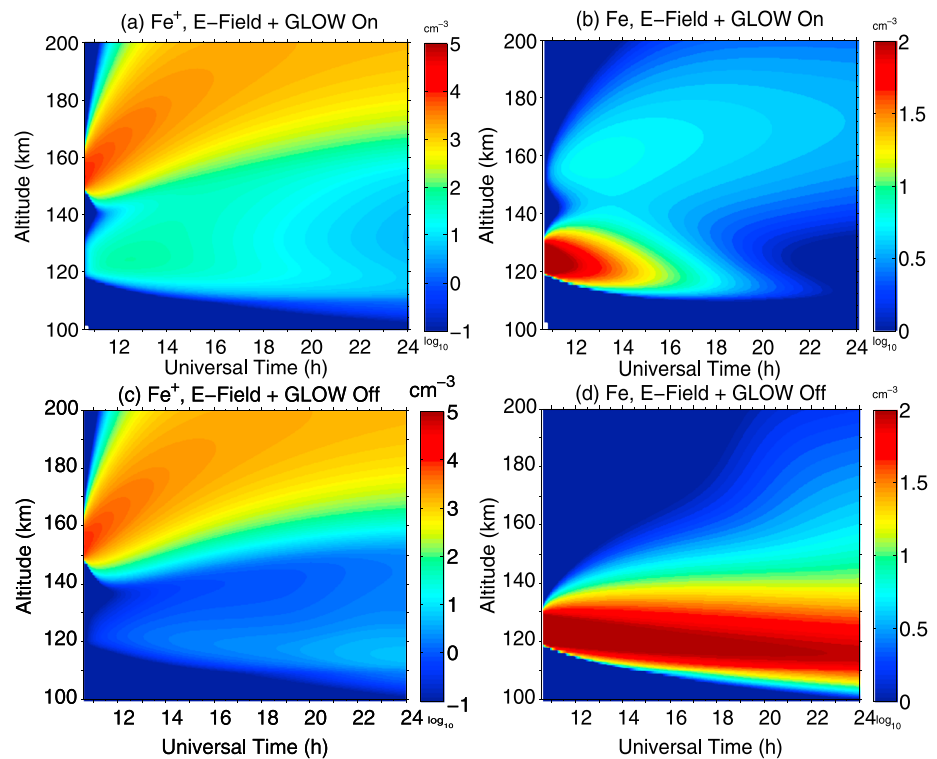


Figure 11. Tests of aurora effects on the thermospheric Fe^+ and Fe layers. (a–d) Variations of Fe^+ or Fe densities in \log_{10} scales versus time and altitude simulated by the TIFE model. Square initial profiles of Fe^+ and Fe densities are used in these simulations. Neutral winds are turned off, but the chemistry model is turned on. The electric field is set to 1 mV/m pointing to geomagnetic east. The GLOW model is turned on for Figures 11a and 11b but off for Figures 11c and 11d.

strengths and phases across multiple factors contribute to the formation of Fe layer shapes. We attempt to reproduce with numerical simulations the Fe layer event observed on 28 May 2011 at McMurdo. This investigation helps illustrate the interplay of multiple factors and determine the relative importance of various factors in forming this stunning event.

5.1. Reproducing the Fe Layer Observations on 28 May 2011

To reproduce the first Fe layer observed at relatively low altitudes around 12 UT, the altitude of the peak density of the initial Fe^+ density profile used in the model is set to around 100 km at a start time of 11 UT (as given in Figure 3a). Figure 3a also shows the initial Fe density profile used in the model. Notice that the Fe density above 110 km is set to zero so that any neutral Fe above 110 km would come from the model simulation. The initial profiles of other iron species (other than Fe and Fe^+) are all set to zero, and the initial environmental neutral and ionic parameters are provided by MSIS and IRI models for the specific date and geomagnetic conditions. The simulation starts at 11 UT and runs only the chemistry module for the first half hour using chemical reactions listed in Tables 1 and 2. As a result, the profiles of all iron species obtained at 11:30 UT with the model are taken as the effective initial profiles used in the following full simulations. The transport module is turned on at 11:30 UT and runs with the chemistry module for 12 h, the same duration as the lidar observation. The time step is set to 1 s, and the data are saved every 2 min. All results shown in this section start at 11:30 UT.

As noted in *Chu et al.* [2011], there was a geomagnetic storm on 28 May 2011 with a Kp index of 6. The average aurora hemispheric power between 11 and 23 UT is about 37.1 GW, which is obtained from the measurements of NOAA POES satellites. The location of McMurdo is near the edge of aurora oval, but very bright aurora was seen overhead during the lidar observations. We take 1.5 erg/s/cm² as the energy flux input to the GLOW model for calculating the particle precipitation and molecular ion densities. The auroral electron spectrum input is set to a Maxwellian distribution with characteristic mode energy of 1 keV and mean energy

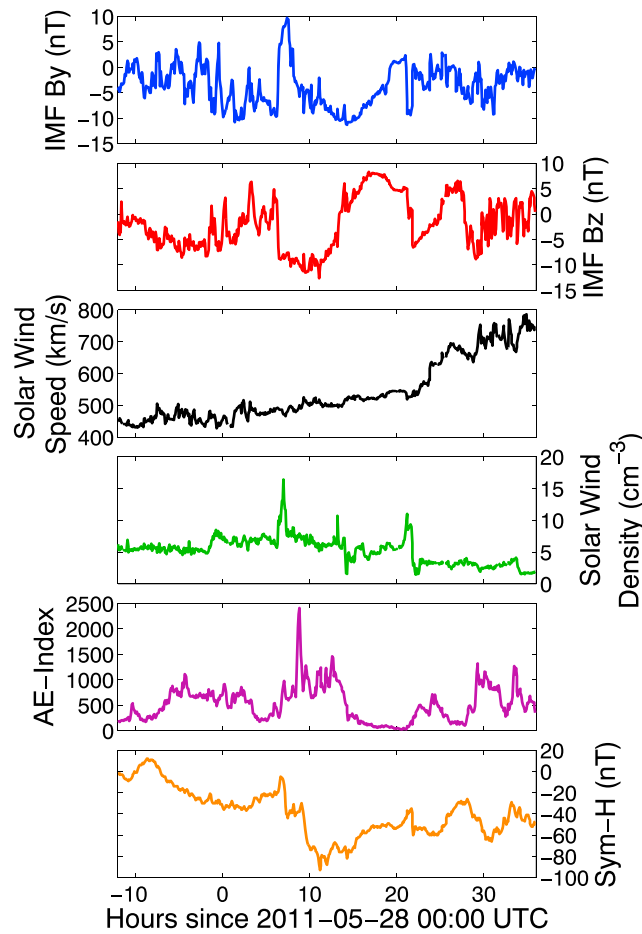


Figure 12. Interplanetary magnetic field (IMF), solar wind, AE index, and SYM-H around 28 May 2011 measured by satellites and magnetometers. Data are downloaded from OMNIWeb (http://omniweb.gsfc.nasa.gov/form/omni_min.html).

and layer shapes can be obtained as demonstrated in Figure 8. Checking the Super Dual Auroral Radar Network (SuperDARN) data [Ruohoniemi and Baker, 1998] (<http://vt.superdarn.org/tiki-index.php?page=ASCIIData>) on 28 May 2011 around the lidar observation time, the interpolated electric field strength near McMurdo is about 50–65% of that computed by Weimer model. Therefore, for reproducing the 28 May 2011 event, the polar electric field is set to 45% of the original Weimer field in Figure 4c for simulations shown in Figures 13–15.

Besides the electric field, neutral winds play important roles in the transport and layering of Fe⁺ and Fe. The observed Fe layers are dominated by gravity waves with periods of ~1.5 h, and the gravity-wave-induced neutral winds are forward modeled in Figure 5b as described in section 3.2. Such short wave-periods along with limited downward transport speeds do not allow sufficient Fe⁺ ions to move below 200 km in time, once they have been transported to very high altitudes. This is also why the electric field has to be cut to 45% as discussed above. Certainly, the background horizontal winds can also play a role and should be added to the wave-induced winds to form the total neutral winds used in equation (8) to calculate the Fe⁺ vertical drift. Unfortunately, at this time there are no good horizontal neutral wind measurements in the simulated altitude ranges (~100 to 500 km), and horizontal wind models do not provide sufficient wind estimates during geomagnetic storms. The mechanism tests in Figures 7 and 8 with zero background winds suggest reasonable results. Therefore, we set the horizontal background winds to zero and take the forward modeled gravity-wave-induced neutral winds in Figure 5b as the total neutral winds in the TIFE model to reproduce the lidar observation.

20.0 eV. The IMF and solar wind data measured by ACE (Advanced Composition Explorer) satellite reveal a coronal mass ejection (CME) event on 28 May 2011 (Figure 12). The IMF B_z from ACE shows a sharp turn from northward to southward between 6 and 7 UT, while the solar wind density shows a sharp peak. The solar wind density varies from 4 to over 10 cm⁻³, and the solar wind velocity changes from 500 to 600 km/s. Driven by the smoothed ACE data, the empirical electric potential model [Weimer, 2005] computes the high-latitude electric potential and magnetic field-aligned current. The electric field strength is then calculated from the electric potential, $\vec{E} = -\nabla\Phi$, for McMurdo location and illustrated in Figure 4c. However, when using the full strength of such electric field in the TIFE model, Fe⁺ ions are uplifted to very high altitudes, leading to low Fe⁺ densities below 200 km as demonstrated in Figures 4 and 7. Consequently, the resulting Fe layers have low densities and long-lasting envelope shapes (see Figure 7d) that are not comparable to the lidar observation. When reducing the electric field strength to 45% of that in Figure 4c, satisfactory Fe densities

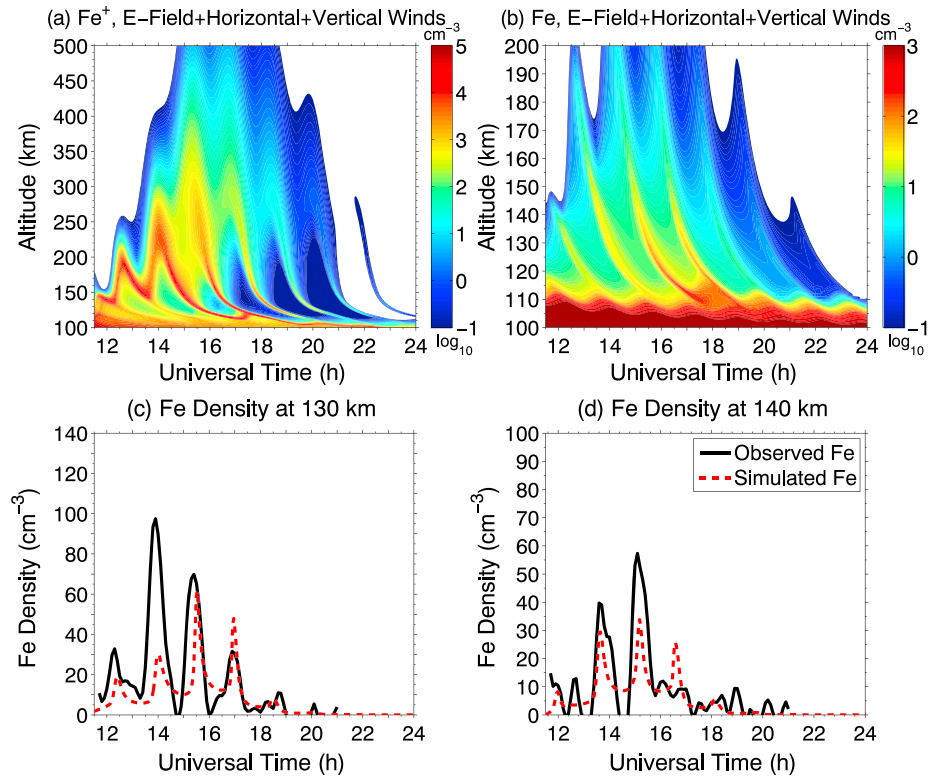


Figure 13. The TIFE model simulations of the thermospheric Fe layer event on 28 May 2011 for McMurdo, Antarctica, with all factors considered together. (a, b) Patterns of Fe^+ and Fe layer densities (in \log_{10} scale) versus time and altitude. (c, d) Comparisons of the simulated and observed Fe layer densities at 130 and 140 km, respectively. The electric field is reduced to 45% of the original strength derived from the Weimer-2005 model. Neutral winds are forward modeled as gravity wave-induced horizontal and vertical winds with zero background winds. The parameterized horizontal divergence is fully counted in. The chemical module is turned on, and the GLOW model is turned on with aurora energy influx of 1.5 erg/s/cm^2 .

Combining all these factors together, the patterns of Fe^+ and Fe layers on 28 May 2011 are simulated and shown in Figures 13a and 13b. We compare the simulation with the observed Fe layers (Figure 3b) from several aspects. First, the curving shapes and gravity wave signatures of the simulated Fe layers in Figure 13b closely resemble the observed Fe layer shape on 28 May 2011 [Chu *et al.*, 2011]. Our tests show that such curving shapes are mainly determined by the profiles of gravity-wave-induced vertical and horizontal winds. Because the wave-induced wind profiles are forward modeled with the observed vertical wavelengths varying with altitudes, the simulated Fe layers are quite close to the observations in this aspect. Second, the simulated overall envelope of the Fe layer shape, especially the change of maximum heights for consecutive Fe layers over time, replicates the observed layer envelope quite well. The Fe layers start at relatively low altitudes, gradually increase the maximum heights for repeated layers, and then decrease the maximum heights until merged with the main Fe layers. Our tests show that such an envelope is determined by three main factors: the initial conditions of Fe^+ density profiles, the electric field, and total neutral winds. In particular, substantial changes of the Fe layer envelope can result if the background horizontal winds are added in the same or opposite direction of the gravity wave propagation. By adjusting the relative phase and strength between the electric field and neutral winds, the Fe layer envelope can be shifted in time and modified in height. Nevertheless, the first layer height is largely determined by the initial Fe^+ density profile. The best simulation results in Figure 13b are obtained with zero background winds, gravity wave-induced neutral winds, 45% electric field strength, and low-altitude initial Fe^+ density profile. Third, the simulated Fe layer “contrast” and width in time are examined in Figures 13c and 13d, where the time series of Fe density variations at 130 and 140 km are compared with the observational data. The contrast of simulated layers is much lower than the contrast in the lidar observation, reflected at the layer troughs where the simulated Fe densities are higher than the observed densities. The layer “width” in time extension is somewhat

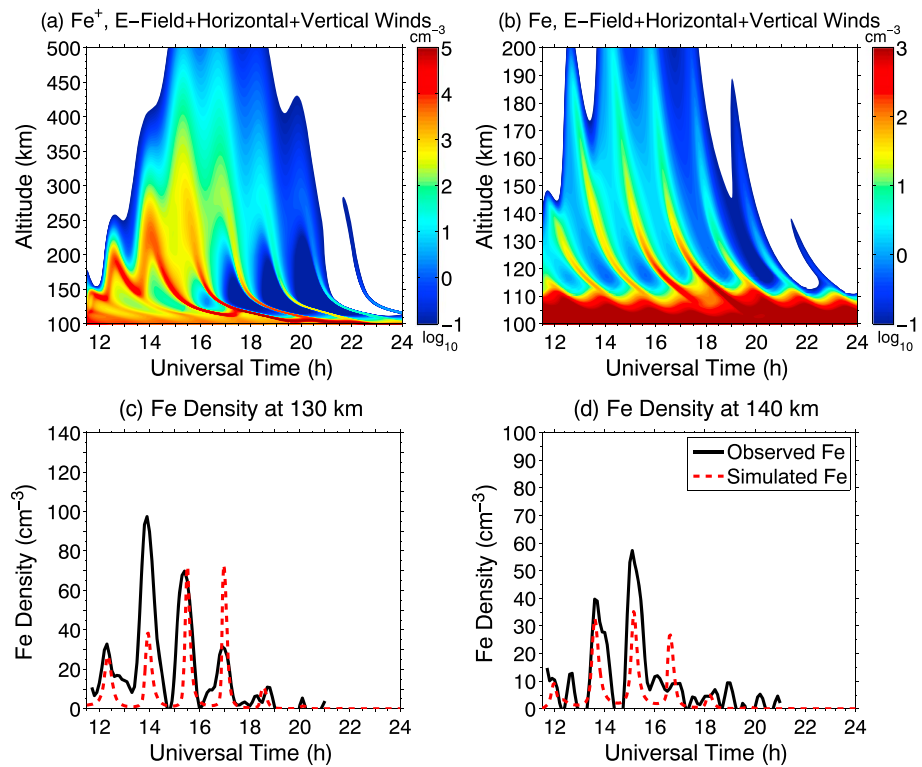


Figure 14. The same as Figure 13 except that the horizontal divergence is turned off for this simulation.

narrower than observations. The peak densities of simulated Fe layers are comparable to observations, and they can be adjusted by varying the initial profiles of Fe⁺ and Fe densities.

5.2. Interplay of Multiple Factors

The above simulations with the full horizontal divergence parameterized exhibit contrast lower than observed. By turning off the horizontal divergence term while keeping all other simulation conditions the same as those in Figure 13, high-contrast Fe layers are obtained as shown in Figure 14. Comparison of the simulated Fe layer densities with observed in Figures 14c and 14d at 130 and 140 km shows a close replication of the lidar-observed Fe layers. Although the Fe contours show large differences between Figures 13b and 14b, the Fe⁺ contours (Figures 13a and 14a) with and without the horizontal divergence term are very similar to each other, except small differences below 120 km. This result can be explained using equations (16) and (17). For Fe⁺, the parentheses terms of equation (17) become much smaller than 1 at higher altitudes, significantly diminishing the effects of horizontal wind divergence. On the contrary, neutral Fe atoms experience the full effects of horizontal wind divergence; e.g., vertical divergence at the troughs induces horizontal convergence, which leads to the difficulty of removing Fe from the troughs, thus the lower contrast in Figure 13. As discussed in section 2.3.3, the horizontal divergence cannot be dismissed; however, it is possible that our parameterized term given by equation (18) may have overestimated the effects. An inference is that for large, horizontally extended layers, the horizontal divergence at the middle of the layers may be partially canceled by the horizontal divergence of the surrounding cells. This is likely the case for the Fe layer event on 28 May 2011, which lasts for many hours, indicating a large horizontal extension of Fe layers, while the lidar beam only has a 100–200 m footprint at 100–200 km altitudes.

Another factor that may affect the layer contrast is the aurora particle precipitation. DMSP observations [Knipp *et al.*, 2014] have indicated that precipitation can be localized, the electron energy distribution may be non-Maxwellian, and significant ion dump in the Southern Hemisphere occurred on 28 May 2011 (Delores J. Knipp, University of Colorado Boulder, private communication). As a result, even under the same aurora hemispheric power, the local energy influx at McMurdo can be many times higher than the mean. To

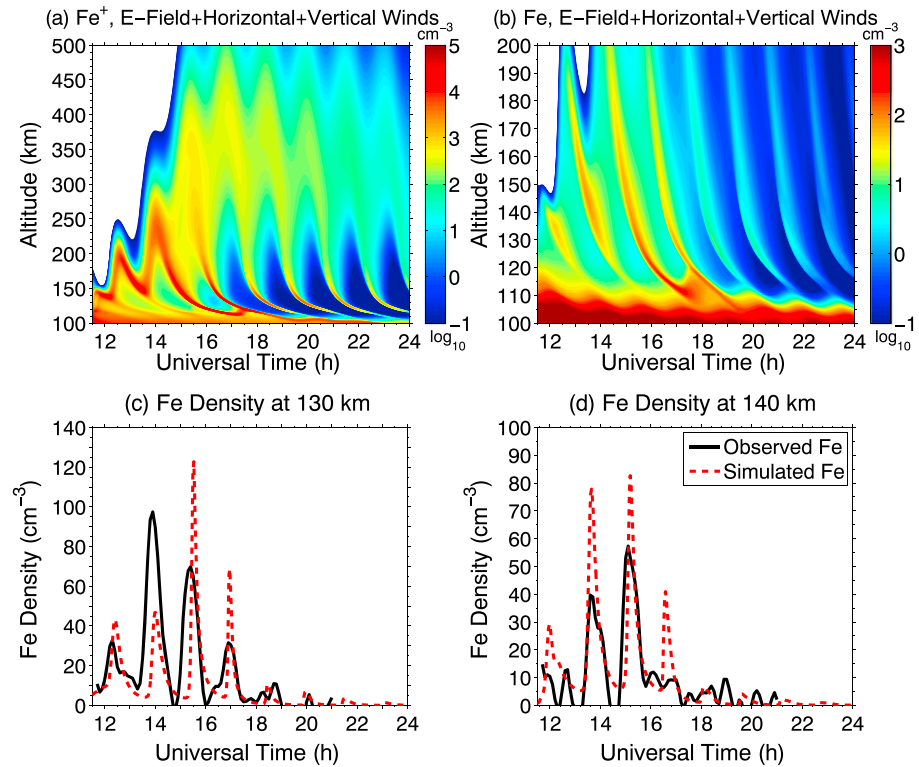


Figure 15. The same as Figure 13 except that the energy influx to the GLOW model is increased to 30 erg/s/cm² for this simulation.

test how such spatially enhanced particle precipitation alters the thermospheric Fe layers, we increase the energy influx in GLOW model by 20 times (from 1.5 to 30 erg/s/cm²) in a new simulation run while keeping all other simulation conditions the same as Figure 13 (including the horizontal divergence term). The results are plotted in Figure 15, where the Fe densities increase at the ridges and decrease at the troughs, leading to significantly improved contrast compared to Figure 13. The long-lasting Fe envelope can be shortened in time if the enhanced energy influx is turned off after the first half run. The tests shown in Figures 14 and 15 indicate that the very high contrast of the thermospheric Fe layers observed on 28 May 2011 may require relatively special conditions to form but low-contrast Fe layers, which have been observed by lidar at McMurdo [Chu et al., 2013, 2016], are readily formed under normal polar conditions.

Overall, the mechanism studies and the TIFE simulations of the 28 May 2011 event demonstrate that multiple factors are at play in shaping neutral Fe layers in the thermosphere. Net production of Fe atoms in the thermosphere occurs wherever the Fe⁺ layer density is sufficiently high so that Fe production via direct and dissociative recombination exceeds Fe loss. Consequently, the altitude, density, and shape of converged Fe⁺ layers strongly affect where and when Fe atoms are produced in the thermosphere and largely determine the maximum heights of Fe layers. However, Fe⁺ layers cannot solely determine the Fe layer shape because once formed from Fe⁺ neutralization, the neutral Fe atoms are no longer subject to Coulomb and Lorentz forces. The motions of Fe atoms are balanced by the neutral winds via collisions and influenced by gravity and diffusion. Separately, Fe⁺ ions are strongly influenced by electromagnetic forces in addition to the neutral winds, gravity, and diffusion. As a result, Fe⁺ motion can deviate from the neutral wind-constrained Fe motion, depending on the electric field strength and direction as well as the neutral wind background. If the electric field is in strong upward or downward phase, it can push the Fe⁺ layers up or down, deviating from the motion of the earlier produced Fe atoms. Once the Fe layer is decoupled from the Fe⁺ layer, the Fe production stops and then net loss of Fe results from charge transfer with NO⁺ and O₂⁺. However, because the Fe⁺ loss due to Fe production is very minor, the remaining Fe⁺ layer still contains sufficiently high density so it continues to produce Fe. Therefore, neutral Fe atoms will be generated at multiple times and locations, which can broaden the observed Fe layers. If the electric field is in the transition from up/downward to

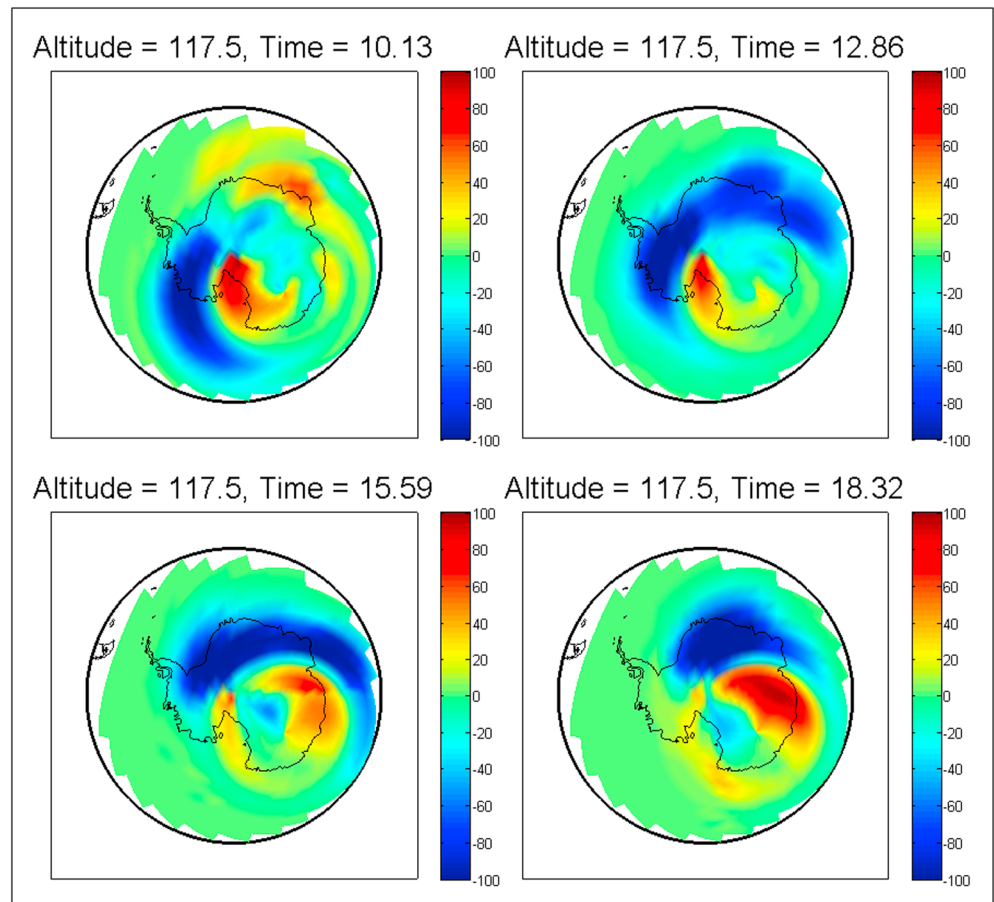


Figure 16. The 2-D map of vertical ion drift velocities for different universal times at altitude of 117.5 km over Antarctica computed by the TIFE model for the conditions on 28 May 2011. The full electric field strength given by the Weimer model is used in the calculation of these 2-D maps. The color bars are in the unit of m/s where the positive (red) represents upward ion transport and the negative (blue) for downward ion flow.

down/upward, the weak electric field will have much less influence on Fe^+ motion. As a result, Fe^+ layers will basically stay with the Fe layers following the neutral winds. In this case, the Fe production can exceed the charge transfer-induced Fe loss, leading to increasing Fe density. In general, because the motion of neutral Fe atoms is mainly driven by the neutral winds, the centers of neutral Fe layers follow the gravity wave phase quite closely when gravity waves dominate the neutral winds, especially the vertical wind. This is true in the region below 200 km where collisions are still frequent enough that gravity and diffusion have minor influences on Fe motions. Furthermore, the aurora particle precipitation can enhance neutralization of Fe^+ in the converged layer by increasing the electron densities, leading to higher Fe densities at the ridges. In the meantime, the aurora-enhanced NO^+ and O_2^+ densities can increase Fe loss via charge transfer once the Fe layers are decoupled from the Fe^+ layers, leading to better depletion of Fe densities at the troughs.

Despite some discrepancy between the simulated and observed Fe layers, the 1-D TIFE model has reproduced the 28 May 2011 event surprisingly well with reasonable density, altitude, wave signature, and evolution shape. This fact indicates that the 1-D TIFE model has captured the major physical mechanisms responsible for the formation of 28 May 2011 Fe layer event. The polar electric field is characterized by diurnal variations of convection pattern of the electric field [Richmond, 1995; Weimer, 2005]. For a single location, the magnitude and direction of electric field has diurnal variations as shown in Figure 4c. Translating to a snap shot over the entire Antarctica, some regions correspond to upward ion motion, while some other regions correspond to downward motion [Iijima and Potemra, 1978]. This point is demonstrated in a simulation shown in Figure 16. In Figure 16, the electric field for every grid point is calculated using the Weimer [2005]

model driven with the IMF and solar wind conditions on 28 May 2011. Then the vertical ion drift velocity for each grid point is calculated using the 1-D TIFe model over the entire Antarctica. It is clear from this 2-D map at altitude of 117.5 km that there are regions of strong downward ion flow and other regions of strong upward flow. Fe^+ can be pushed down and accumulated at relatively lower altitudes in the downward flow regions. Once horizontally advected to McMurdo, such regions can provide the needed initial profiles as in Figure 3a. For the Fe layer event on 28 May 2011, the upward vertical transport of an “extended ion clouds” (the red contour near the lower center of the images) exists for many hours above McMurdo Station, indicating vertical transport as the dominant transport for this event. Consequently, the 1-D TIFe model is well suited to simulate this event by accurately modeling the vertical transport. It is necessary for future TIFe models to include 3-D transport in order to reproduce many other thermospheric Fe layer events observed by lidar in Antarctica [Chu *et al.*, 2016].

6. Conclusions

A thermosphere-ionosphere Fe/Fe⁺ (TIFe) model has been developed from first principles at the University of Colorado to study the formation mechanisms of neutral Fe layers in the thermosphere observed by lidar over McMurdo, Antarctica. In general, the TIFe model simulations confirm and mathematically formulate the TIFe theory proposed by Chu *et al.* [2011] that thermospheric Fe layers with gravity wave signatures are produced through neutralization of Fe⁺ ion layers that are vertically converged by gravity wave-induced vertical shears of vertical and horizontal winds. This study develops the TIFe theory into a numerical TIFe model depicting the lifecycle of meteoric metallic ions and atoms via deposition, transport, chemistry, and wave dynamics. Through mechanism tests and reproductions of a stunning Fe layer event on 28 May 2011, a comprehensive picture is envisaged as follows and illustrated in Figure 1 for the formation of thermospheric Fe layers with clear downward phase progression of atmospheric waves in the polar thermosphere.

1. Upward Transport of Meteoric Fe⁺ Ions From the Main Deposition Region

The polar electric field transports metallic ions Fe⁺ upward from their main deposition region (~80–110 km) into the *E* and *F* regions, providing the major source of Fe⁺ (and accordingly Fe) in the thermosphere. Direct deposition of iron species by meteor ablation and sputtering above 120 km can provide an additional source but is not a necessary and likely not a sufficient condition. The neutral winds can also transport Fe⁺ in the vertical direction. Due to the high magnetic inclination angle, the vertical wind can induce vertical ion drift with magnitudes similar to or even larger than those caused by the horizontal winds, despite the smaller amplitude of vertical wind. The maximum heights of Fe⁺ and transport timing are determined via the combined effects of the electric field strength and direction, neutral wind amplitude and direction, and relative phase relation between the electric field and neutral winds. By adjusting the relative phase and strength between the electric field and neutral winds, the Fe⁺ layer shape can be shifted in time and modified in altitude.

2. Convergence of Fe⁺ Ion Layers in the E-F Regions

Atmospheric (gravity or tidal) wave-induced vertical shears of both vertical and horizontal winds converge the Fe⁺ ions to form dense Fe⁺ layers in the presence of the polar electric field. The electric field in the polar region can converge, diverge, upward transport or downward transport ions, depending on its direction with respect to the geomagnetic field. A southwest directed electric field can produce tight convergence, while under appropriate conditions convergence can also occur for southeast or northwest directed electric fields. However, the clearly apparent wave signatures can only be generated by wind shear mechanisms, as they cannot be explained by the electric field alone. The nature of atmospheric waves that produce the wind shears and vertical wind determines the wave signatures to be gravity or tidal waves. In the case of the McMurdo 28 May 2011 event showing ~1.5 h gravity waves, the vertical shear of vertical wind is as effective as that of horizontal winds in converging Fe⁺ ions. The relative phase and strength between the convection electric field and the wave-induced neutral winds determine whether converged Fe⁺ ion layers can be formed at certain locations and the occurrence times and altitudes of Fe and Fe⁺ layers.

3. Neutralization of Fe⁺ Ions to Form Fe Atoms

Direct electron-Fe⁺ recombination (via RR and DR) is the major channel to neutralize converged Fe⁺ ions to form neutral Fe atoms in the upper *E* and *F* regions. Below ~125 km, both direct and dissociative

recombination processes contribute to neutral Fe production. The altitudes for dissociative recombination to be effective are mainly determined by the O_3 distribution profiles. Though only $\sim 0.1\%$ of Fe^+ is converted to Fe, this is sufficient to produce an Fe density detectable by lidar. Auroral particle precipitation plays double-edged sword roles. The energetic electron fluxes produced by diffusive aurora enhance the electron densities in the E - F regions, accelerating the production of Fe via neutralization of Fe^+ in converged layers. At the same time, aurora increases the loss of Fe via enhanced charge transfer with increased densities of NO^+ , O_2^+ , and O^+ and via ionization by aurora electron impact, especially when the Fe layers are decoupled from the Fe^+ layers. The overall effect is that aurora particle precipitation enhances the TIFE layer contrast by producing higher Fe densities at the ridges and lower Fe densities in the troughs.

4. Evolution of Fe Layer Shapes Under Multiple Factors

Fe layer shapes are determined by multiple factors. The altitude, density, and shape of converged Fe^+ layers largely determine where and when Fe atoms are produced in the thermosphere, but Fe^+ layers cannot solely determine the Fe layer shapes. This is because once formed, the neutral Fe are no longer subject to electromagnetic forces but are balanced by neutral winds, gravity, and diffusion. The gravity wave-induced vertical wind plays a key role in shaping the neutral Fe layers to form the observed gravity wave signatures with downward phase progression on 28 May 2011 at McMurdo. The overall envelope of the thermospheric Fe layers is determined by the initial Fe^+ density profile, the electric field, and total 3-D neutral winds. The changes of relative phase and strength between the neutral winds and electric field can alter the Fe layer envelope in timing and altitude. If Fe^+ and Fe layers stay together due to the weak electric field during direction transition, the Fe production can exceed loss, leading to increased Fe density. If a strong electric field deviates Fe^+ from the Fe layer, the remaining Fe^+ layer can continue producing Fe but at different locations than before. Once decoupled from Fe^+ , the Fe layers experience net loss mainly due to charge transfer with NO^+ and O_2^+ , which can be enhanced by aurora particle precipitation.

This study presents the first quantitative investigation of the formation mechanisms of thermospheric neutral metal layers with the TIFE model, which not only formulates the theory originally proposed by *Chu et al.* [2011] but also provides further insights on the aspects of polar electric field in transporting Fe^+ ions, neutral wind shears in converging Fe^+ layers, and wave-induced vertical wind in shaping the Fe layers as well as aurora roles in the formation of Fe layers in the thermosphere. The mechanisms formulated in this study represent the major formation mechanisms responsible for thermospheric Fe layers, such as those observed on 2 and 28 May 2011, with clear downward phase progression of gravity waves [*Chu et al.*, 2011]. It is necessary to point out that this study does not rule out the possibility that the Joule heating-induced neutral upwelling can contribute to the formation of neutral metal layers in the thermosphere. Aurora heating may cause upwelling that can transport neutrals (including Fe) upward from the meteor deposition region into the thermosphere. With frequent ion-neutral collisions at these low altitudes, such neutral upwelling may also help uplift Fe^+ ions to the E region. TIFE model simulations, without considering such neutral upwelling, have reproduced the major features of the event on 28 May 2011, indicating that this mechanism does not need to play a major role in such events. However, this neutral upwelling mechanism may be responsible for some other forms of the thermospheric Fe layers, for example, lidar observations of upward phase progression in thermospheric Fe layers [*Chu et al.*, 2016]. The TIFE model provides a framework for such an investigation since the Joule heating-induced neutral upwelling can be implemented via adding to the neutral wind models as an input to the TIFE model, which will be a topic of future study. It is also worth noting that direct deposition of metallic ions and neutrals by sputtering of fast meteoroids can provide additional sources to the Fe^+ and Fe abundance in the thermosphere. The resulting additional ions will undergo the same transport, convergence, and neutralization processes as described above. Nonetheless, wave perturbations of the directly deposited neutral metals alone are unlikely to produce sufficiently high contrast as observed.

Although currently focusing on Fe species in the polar region, the TIFE theory formulated in this study can be extrapolated to help infer a global picture of multiple metal species. A common point is the plasma-neutral coupling between ionic and neutral metals; i.e., the observed neutral metals with apparent wave signatures are produced via neutralization of vertically converged metal ion layers, mainly through the direct recombination $Mt^+ + e^- \rightarrow Mt + h\nu$ above ~ 120 km [*Plane et al.*, 2015]. The upward transport, convergence, and neutralization of metal ions Mt^+ are the major steps to form neutral metal (Mt) layers in the E and lower F regions

globally, while the evolution of neutral Mt layers is determined by multiple factors as demonstrated in this study for neutral Fe layers. Two major differences are introduced when comparing low latitudes with the polar regions: (1) the fountain effect of the equatorial electric field substitutes for the polar electric field in the upward transport of metal ions (Na^+ , K^+ , Fe^+ , etc.) from their main deposition region to the E - F regions and (2) gravity-wave-dominated wind shears are replaced by tidal-wave-driven wind shears. Because the geomagnetic field is nearly horizontal at low latitudes, the vertical shears of horizontal winds play the major role in converging metal ions into dense layers, while the vertical wind effects largely diminish. Both Lijiang and Cerro Pachon are within the fountain effect region and have tidal waves dominating the thermospheric wind fields. Therefore, the global picture inferred above can help explain the observations at both locations showing apparent tidal phases [Gao *et al.*, 2015; Smith and Chu, 2015; Liu *et al.*, 2016]. In a previous publication [Gao *et al.*, 2015], we have done such extrapolation to provide a qualitative explanation to the lidar observations of neutral Na layers up to 170 km at Lijiang, China, where the equatorial fountain effect replaces the polar electric field for the transport of Na^+ ions. Because of the different electric fields at different latitudes, the distribution and occurrence of thermospheric neutral metal layers are mainly determined by the transport of metallic ions from their main deposition region to the E - F regions. Accordingly, the polar and low latitudes will experience more frequent occurrence of neutral metal layers in the thermosphere because the polar electric field and equatorial fountain effect are effective in upward transporting metal ions, while middle latitudes experience less. This inference is consistent with the satellite observations of Mg^+ , Ca^+ , and Na [Gardner *et al.*, 1999] and with ground-based lidar observations to date. It is worth pointing out that thermospheric metal layers can still occur at midlatitudes as a Na layer has been observed up to 160 km at Beijing, China (Qi Gao, private communication, University of Science and Technology of China), although such events are rare so far.

Certainly, such a global picture for multiple metal species must be quantitatively investigated with future numerical simulations and global observations from the ground and space. Expanding the current TIFE model into a global model and incorporating multiple metal species (e.g., Na, K, Mg, Ca, Ni, and Al), in addition to Fe, are two main future directions. Various metallic ions will experience similar electromagnetic forces, but there are large mass differences between them (e.g., Fe/Fe^+ are much heavier than the mean air molecules, while Na/Na^+ are lighter). In addition, different sets of chemical reactions govern the conversions among different metals and their molecular species. All these factors must be quantitatively modeled to evaluate their effects on the formation of thermospheric metal layers. Furthermore, it is impractical for the 1-D model to handle horizontal transport of metal layers comprehensively. The dense Fe^+ layers are not necessarily a result of the vertical convergence only, but horizontal convergence and horizontal transport induced by convection electric field and neutral background wind can contribute to their formation, which should be modeled in three dimensions. The parameterized horizontal wind divergence in the 1-D model should also be fully resolved in a 3-D model for accurately accounting its effects on the converged Fe^+ and Fe layers. This term appears to be a major uncertainty in the TIFE model, affecting the Fe layer contrast. Necessary steps for the future may include (1) developing the TIFE model into a self-consistent 3-D model, (2) implementing the TIFE model into an existing 3-D general circulation model (GCM), or (3) more practically expanding the TIFE model to a 3-D chemical transport model that will be driven by a 3-D GCM. Finally, the future 3-D model should include energetics, allowing studies of the Joule heating and other plasma-neutral coupling effects associated with the thermospheric metal layer events. Global simultaneous observations of thermospheric metal layers and their ion layers along with electrons are crucial to verify the TIFE theory and model simulations. With modern high-performance resonance-fluorescence Doppler and Boltzmann lidars, these neutral metal layers provide excellent tracers for direct measurements of neutral winds and temperatures in the thermosphere and provide a unique natural laboratory for understanding the fundamental processes critical to advancing the research of space-atmosphere interactions.

References

- Aikin, A. C., and H. J. P. Smith (1999), Mesospheric constituent variations during electron precipitation events, *J. Geophys. Res.*, *104*(D21), 26,457–26,471, doi:10.1029/1999JD900752.
- Allen, M., J. I. Lunine, and Y. L. Yung (1984), The vertical distribution of ozone in the mesosphere and lower thermosphere, *J. Geophys. Res.*, *89*(D3), 4841–4872, doi:10.1029/JD089iD03p04841.
- Axford, W. I. (1963), The formation and vertical movement of dense ionized layers in the ionosphere due to neutral wind shears, *J. Geophys. Res.*, *68*(3), 769–779, doi:10.1029/JZ068i003p00769.

Acknowledgments

We gratefully acknowledge Arthur D. Richmond for invaluable guidance in formulating the TIFE theory and for numerous discussions on parameterizing the horizontal wind divergence. We appreciate John M.C. Plane, Wuhu Feng, and Juan Diego Carrillo-Sánchez for invaluable advice on Fe/Fe^+ chemistry and cosmic dust ablation/sputtering and for providing many reaction rate coefficients. We are grateful to Jeffery M. Forbes and Rebecca L. Bishop for providing the Carter and Forbes model framework and for invaluable discussions on the model development; to Stanley C. Solomon, Hanli Liu, Daniel R. Weimer, and Ben Foster for providing the GLOW, TIME-GCM, and Weimer-2005 models; and to Sharon L. Vadas and Cao Chen for discussions on setting up the gravity wave forward model. We are indebted to Timothy J. Fuller-Rowell, Delores J. Knipp, and Zhonghua Xu for invaluable discussions on ionospheric electrodynamics, DMSP observations, and geomagnetic storms. We are grateful to Zhonghua Xu for his advice in interpreting the SuperDARN data, to Liam M. Kilcommons for his help in producing Figure 12 with OMNI data, to Jian Zhao for finding a coding error in the electric field calculation, and to Jonathan S. Friedman and Muzhou Lu for English editing and scientific feedback. We sincerely acknowledge Vladimir Papitashvili and Julie Palais for their encouragement, guidance, and discussions in pursuing the TIFE subject. We appreciate the staff of the United States Antarctic Program, McMurdo Station, Antarctica New Zealand, and Scott Base for their superb support to the McMurdo lidar observations. We acknowledge the NASA Space Science Data facility for the OMNI data from the GSFC/SPDF OMNIWeb interface at (<http://omniweb.gsfc.nasa.gov>). We acknowledge the use of the “Map Potential Plot” tool hosted by the Virginia Tech SuperDARN group at their website (<http://vt.superdarn.org/tiki-index.php?page=DaViT+Map+Potential+Plot>). This project was supported by the National Science Foundation (NSF) grants ANT-0839091 and PLR-1246405.

- Bailey, S. M., C. A. Barth, and S. C. Solomon (2002), A model of nitric oxide in the lower thermosphere, *J. Geophys. Res.*, *107*(A8), 1205, doi:10.1029/2001JA000258.
- Banks, P. M., and G. Kockarts (1973), *Aeronomy. Part B*, pp. 32–63, Academic Press, New York.
- Bautista, M. A., P. Romano, and A. K. Pradhan (1998), Resonance-averaged photoionization cross sections for astrophysical models, *Astrophys. J. Suppl. Ser.*, *118*, 259–265, doi:10.1086/313132.
- Billitza, D., L.-A. McKinnell, B. Reinisch, and T. Fuller-Rowell (2011), The international reference ionosphere (IRI) today and in the future, *J. Geod.*, *85*, 909–920, doi:10.1007/s00190-010-0427-x.
- Bishop, R. L., and G. D. Earle (2003), Metallic ion transport associated with midlatitude intermediate layer development, *J. Geophys. Res.*, *108*(A1), 1019, doi:10.1029/2002JA009411.
- Bones, D. L., J. M. C. Plane, and W. Feng (2016), Dissociative recombination of FeO^+ with electrons: Implications for plasma layers in the ionosphere, *J. Phys. Chem. A*, *120*, 1369–1376, doi:10.1021/acs.jpca.5b04947.
- Boris, J. P., and D. L. Book (1973), Flux-corrected transport: I. SHASTA, a fluid transport algorithm that works, *J. Comput. Phys.*, *11*, 38–69.
- Brasseur, G. P., and S. Solomon (2005), *Aeronomy of the Middle Atmosphere—Chemistry and Physics of the Stratosphere and Mesosphere*, 3rd ed., pp. 51–149, Springer, Dordrecht, Netherlands.
- Brekke, A. (2013), *Physics of the Upper Polar Atmosphere*, 2nd ed., pp. 189–245, Springer, Berlin, Heidelberg, doi:10.1007/978-3-642-27401-5.
- Bristow, W. A., and B. J. Watkins (1991), Numerical simulation of the formation of thin ionization layers at high latitudes, *Geophys. Res. Lett.*, *18*, 404–407, doi:10.1029/90GL02588.
- Brown, P. N., A. C. Hindmarsh, and L. R. Petzold (1994), Using Krylov methods in the solution of large-scale differential-algebraic systems, *SIAM J. Sci. Comput.*, *15*, 1467–1488, doi:10.1137/0915088.
- Burns, A. G., T. L. Killeen, and R. G. Roble (1991), A theoretical study of thermospheric composition perturbations during an impulsive geomagnetic storm, *J. Geophys. Res.*, *96*, 14,153–14,167, doi:10.1029/91JA00678.
- Carrillo-Sánchez, J. D., J. M. C. Plane, W. Feng, D. Nesvorný, and D. Janches (2015), On the size and velocity distribution of cosmic dust particles entering the atmosphere, *Geophys. Res. Lett.*, *42*, 6518–6525, doi:10.1002/2015GL065149.
- Carrillo-Sánchez, J. D., D. Nesvorný, P. Pokorný, D. Janches, and J. M. C. Plane (2016), Sources of cosmic dust in the Earth's atmosphere, *Geophys. Res. Lett.*, *43*, 11,979–11,986, doi:10.1002/2016GL071697.
- Carter, L. N. J. (1995), A comprehensive model of global transport and localized layering of metallic ions in the upper atmosphere, PhD thesis, Boston Univ., Boston, Mass.
- Carter, L. N., and J. M. Forbes (1999), Global transport and localized layering of metallic ions in the upper atmosphere, *Ann. Geophys.*, *17*, 190–209, doi:10.1007/s00585-999-0190-6.
- Chen, A., R. Johnsen, and M. A. Biondi (1978), Measurements of the $\text{O}^+ + \text{N}_2$ and $\text{O}^+ + \text{O}_2$ reaction rates from 300 to 900 K, *J. Chem. Phys.*, *69*, 2688–2691.
- Chu, X., Z. Yu, C. S. Gardner, C. Chen, and W. Fong (2011), Lidar observations of neutral Fe layers and fast gravity waves in the thermosphere (110–155 km) at McMurdo (77.8°S, 166.7°E), Antarctica, *Geophys. Res. Lett.*, *38*, L23807, doi:10.1029/2011GL050016.
- Chu, X., Z. Yu, W. Fong, C. Chen, C. S. Gardner, B. R. Roberts, X. Lu, and T. J. Fuller-Rowell (2013), Lidar observations of thermospheric Fe layers, temperatures and gravity waves at McMurdo, Antarctica, paper presented at Coupling, Energetics and Dynamics of Atmospheric Regions (CEDAR) Workshop, Boulder, Colo.
- Chu, X., Z. Yu, W. Fong, C. Chen, J. Zhao, I. F. Barry, J. A. Smith, X. Lu, W. Huang, and C. S. Gardner (2016), From Antarctica lidar discoveries to OASIS exploration, EPJ Web of Conferences, 119, 12001, invited paper in Proceedings of the 27th International Laser Radar Conference, New York, July 2015, doi:10.1051/epjconf/201611912001.
- Collins, S. C., et al. (2002), A study of the role of ion-molecule chemistry in the formation of sporadic sodium layers, *J. Atmos. Sol. Terr. Phys.*, *64*, 845–860.
- Delgado, R., J. S. Friedman, J. T. Fentzke, S. Raizada, C. A. Tepley, and Q. Zhou (2012), Sporadic metal atom and ion layers and their connection to chemistry and thermal structure in the mesopause region at Arecibo, *J. Atmos. Sol. Terr. Phys.*, *74*, 11–23, doi:10.1016/j.jastp.2011.09.004.
- Djuth, F. T., L. D. Zhang, D. J. Livneh, I. Seker, S. M. Smith, M. P. Sulzer, J. D. Mathews, and R. L. Walterscheid (2010), Arecibo's thermospheric gravity waves and the case for an ocean source, *J. Geophys. Res.*, *115*, A08305, doi:10.1029/2009JA014799.
- Durrant, D. R. (2010), *Numerical Methods for Fluid Dynamics With Applications to Geophysics*, 2nd ed., pp. 203–280, Springer, New York, doi:10.1007/978-1-4419-6412-0.
- Earle, G. D., T. J. Kane, R. F. Pfaff, and S. R. Bounds (2000), Ion layer separation and equilibrium zonal winds in midlatitude sporadic E, *Geophys. Res. Lett.*, *27*, 461–464, doi:10.1029/1999GL900572.
- Fang, X., C. E. Randall, D. Lummerzheim, S. C. Solomon, M. J. Mills, D. R. Marsh, C. H. Jackman, W. Wang, and G. Lu (2008), Electron impact ionization: A new parameterization for 100 eV to 1 MeV electrons, *J. Geophys. Res.*, *113*, A09311, doi:10.1029/2008JA013384.
- Fazio, R., and A. Jannelli (2009), Second order numerical operator splitting for 3D advection-diffusion-reaction models, in *Numerical Mathematics and Advanced Applications 2009*, edited by G. Kreiss et al., pp. 317–324, Springer, Berlin Heidelberg, doi:10.1007/978-3-642-11795-4_33.
- Fehsenfeld, F. C. (1977), The reaction of O_2^+ with atomic nitrogen and $\text{NO}^+ \cdot \text{H}_2\text{O}$ and NO_2^+ with atomic oxygen, *Planet. Space Sci.*, *25*, 195–196, doi:10.1016/0032-0633(77)90025-3.
- Feng, W., D. R. Marsh, M. P. Chipperfield, D. Janches, J. Höffner, F. Yi, and J. M. C. Plane (2013), A global atmospheric model of meteoric iron, *J. Geophys. Res. Atmos.*, *118*, 9456–9474, doi:10.1002/jgrd.50708.
- Finlay, C. C., et al. (2010), International Geomagnetic Reference Field: The eleventh generation, *Geophys. J. Int.*, *183*, 1216–1230.
- Frahm, R. A., J. D. Winningham, J. R. Sharber, R. Link, G. Crowley, E. E. Gaines, D. L. Chenette, B. J. Anderson, and T. A. Potemra (1997), The diffuse aurora: A significant source of ionization in the middle atmosphere, *J. Geophys. Res.*, *102*(D23), 28,203–28,214, doi:10.1029/97JD02430.
- Fritts, D. C., and M. J. Alexander (2003), Gravity wave dynamics and effects in the middle atmosphere, *Rev. Geophys.*, *41*(1), 1003, doi:10.1029/2001RG000106.
- Friedman, J. S., X. Chu, C. Brum, and X. Lu (2013), Observation of a thermospheric descending layer of neutral K over Arecibo, *J. Atmos. Sol. Terr. Phys.*, *104*, 253–259, doi:10.1016/j.jastp.2013.03.002.
- Gao, Q., X. Chu, X. Xue, X. Dou, T. Chen, and J. Chen (2015), Lidar observations of thermospheric Na layers up to 170 km with a descending tidal phase at Lijiang (26.7°N, 100.0°E), China, *J. Geophys. Res. Space Physics*, *120*, 9213–9220, doi:10.1002/2015JA021808.
- Gardner, C. S., A. Z. Liu, D. R. Marsh, W. Feng, and J. M. C. Plane (2014), Inferring the global cosmic dust influx to the Earth's atmosphere from lidar observations of the vertical flux of mesospheric Na, *J. Geophys. Res. Space Physics*, *119*, 7870–7879, doi:10.1002/2014JA020383.
- Gardner, J. A., A. L. Broadfoot, W. J. McNeil, S. T. Lai, and E. Murad (1999), Analysis and modeling of the GLO-1 observations of meteoric metals in the thermosphere, *J. Atmos. Sol. Terr. Phys.*, *61*, 545–562.

- Gossard, E. E., and W. H. Hooke (1975), *Waves in the Atmosphere: Atmospheric Infrasound and Gravity Waves—Their Generation and Propagation*, pp. 27–87, Elsevier Scientific Pub. Co., Amsterdam.
- Grebowksy, J. M., and H. C. Brinton (1978), Fe⁺ ions in the high latitude F-region, *Geophys. Res. Lett.*, *5*(9), 791–794, doi:10.1029/GL005i009p00791.
- Grebowksy, J., and M. Pharo (1985), The source of midlatitude metallic ions at F-region altitudes, *Planet. Space Sci.*, *33*(7), 807–815, doi:10.1016/0032-0633(85)90034-0.
- Grebowksy, J. M., and A. C. Aikin (2002), In situ measurements of meteoric ions, in *Meteors in the Earth's Atmosphere*, edited by E. Murad and I. P. Williams, pp. 189–214, Cambridge Univ. Press, New York.
- Green, A. E. S., and T. Sawada (1972), Ionization cross sections and secondary electron distributions, *J. Atmos. Terr. Phys.*, *34*, 1719–1728.
- Helmer, M., and J. M. C. Plane (1994), Kinetic study of the reaction between Fe and O₃ under mesospheric conditions, *J. Chem. Soc., Faraday Trans.*, *90*, 31–37.
- Helmer, M., J. M. C. Plane, J. Qian, and C. S. Gardner (1998), A model of meteoric iron in the upper atmosphere, *J. Geophys. Res.*, *103*(D9), 10,913–10,925, doi:10.1029/97JD03075.
- Höffner, J., and J. S. Friedman (2005), The mesospheric metal layer topside: Examples of simultaneous metal observations, *J. Atmos. Sol. Terr. Phys.*, *67*, 1226–1237.
- Huang, W., X. Chu, C. S. Gardner, J. D. Carrillo-Sánchez, W. Feng, J. M. C. Plane, and D. Nesvorný (2015), Measurements of the vertical fluxes of atomic Fe and Na at the mesopause: Implications for the velocity of cosmic dust entering the atmosphere, *Geophys. Res. Lett.*, *42*, 169–175, doi:10.1002/2014GL062390.
- Iijima, T., and T. A. Potemra (1978), Large-scale characteristics of field-aligned currents associated with substorms, *J. Geophys. Res.*, *83*(A2), 599–615, doi:10.1029/JA083iA02p00599.
- Jensen, D. E., and G. A. Jones (1974), Catalysis of radical recombination in flames by iron, *J. Chem. Phys.*, *60*, 3421–3425.
- Khan, L. A., and P. L. F. Liu (1995), An operator splitting algorithm for coupled one-dimensional advection-diffusion-reaction equations, *Comput. Methods Appl. Mech. Eng.*, *127*(1–4), 181–201.
- Knipp, D. J., T. Matsuo, L. Kilcommons, A. Richmond, B. Anderson, H. Korth, R. Redmon, B. Mero, and N. Parrish (2014), Comparison of magnetic perturbation data from LEO satellite constellations: Statistics of DMSP and AMPERE, *Space Weather*, *12*, 2–23, doi:10.1002/2013SW000987.
- Kopp, E. (1997), On the abundance of metal ions in the lower ionosphere, *J. Geophys. Res.*, *102*(A5), 9667–9674, doi:10.1029/97JA00384.
- Langford, A. O., V. M. Bierbaum, and S. R. Leone (1985), Auroral implications of recent measurements on O(¹S) and O(¹D) formation in the reaction of N⁺ with O₂, *Planet. Space Sci.*, *33*, 1225–1228, doi:10.1016/0032-0633(85)90078-9.
- Larsen, M. F., and J. W. Meriwether (2012), Vertical winds in the thermosphere, *J. Geophys. Res.*, *117*, A09319, doi:10.1029/2012JA017843.
- Li, Y., J. G. Luhmann, B. J. Lynch, and E. K. J. Kilpua (2014), Magnetic clouds and origins in STEREO era, *J. Geophys. Res. Space Physics*, *119*, 3237–3246, doi:10.1002/2013JA019538.
- Lindinger, W., and E. Ferguson (1983), Laboratory investigation of the ionospheric O₂⁺ (X²Π_g, v = 0) reaction with NO, *Planet. Space Sci.*, *31*, 1181–1182.
- Liu, A. Z., Y. Guo, F. Vargas, and G. R. Swenson (2016), First measurement of horizontal wind and temperature in the lower thermosphere (105–140 km) with a Na Lidar at Andes Lidar Observatory, *Geophys. Res. Lett.*, *43*, 2374–2380, doi:10.1002/2016GL068461.
- Lui, A. T. Y., P. Perreault, S.-I. Akasofu, and C. D. Anger (1973), The diffuse aurora, *Planet. Space Sci.*, *21*, 857–861.
- Lübken, F.-J., J. Höffner, T. P. Viehl, B. Kaifler, and R. J. Morris (2011), First measurements of thermal tides in the summer mesopause region at Antarctic latitudes, *Geophys. Res. Lett.*, *38*, L24806, doi:10.1029/2011GL050045.
- MacDougall, J. W., J. M. C. Plane, and P. T. Jayachandran (2000), Polar cap sporadic-E: Part 2. Modeling, *J. Atmos. Sol. Terr. Phys.*, *62*, 1169–1176.
- MacLeod, M. A., T. J. Keneshea, and R. S. Narcisi (1975), Numerical modelling of a metallic ion sporadic-E layer, *Radio Sci.*, *10*(3), 371–388, doi:10.1029/RS010i003p00371.
- Mathews, J., and F. Bekeny (1979), Upper atmosphere tides and the vertical motion of ionospheric sporadic layers at Arecibo, *J. Geophys. Res.*, *84*(A6), 2743–2750, doi:10.1029/JA084iA06p02743.
- Mathews, J. D. (1998), Sporadic E: Current views and recent progress, *J. Atmos. Sol. Terr. Phys.*, *60*, 413–435.
- McFarland, M., D. L. Albritton, F. C. Fehsenfeld, E. E. Ferguson, and A. L. Schmeltekopf (1973), Flow-drift technique for ion mobility and ion-molecule reaction rate constant measurements: II. Positive ion reactions of N⁺, O⁺, and N₂⁺ with O₂ and O⁺ with N₂ from thermal to ~2 eV, *J. Chem. Phys.*, *59*, 6620–6628.
- McFarland, M., D. L. Albritton, F. C. Fehsenfeld, E. E. Ferguson, and A. L. Schmeltekopf (1974), Energy dependence and branching ratio of the N₂⁺ + O reaction, *J. Geophys. Res.*, *79*, 2925–2926, doi:10.1029/JA079i019p02925.
- Mul, P. M., and J. W. McGowan (1979), Merged electron-ion beam experiments: III. Temperature dependence of dissociative recombination for atmospheric ions NO⁺, O₂⁺, and N₂⁺, *J. Phys. B: At. Mol. Phys.*, *12*, 1591–1601.
- Nagy, A. F., and P. M. Banks (1970), Photoelectron fluxes in the ionosphere, *J. Geophys. Res.*, *75*(31), 6260–6270, doi:10.1029/JA075i031p06260.
- Nahar, S. N., M. A. Bautista, and A. K. Pradhan (1997), Electron-ion recombination of neutral iron, *Astrophys. J.*, *479*, 497–503.
- Nygrén, T., L. Jalonon, J. Oksman, and T. Turunen (1984), The role of electric field and neutral wind direction in the formation of sporadic E-layers, *J. Atmos. Terr. Phys.*, *46*(4), 373–381, doi:10.1016/0021-9169(84)90122-3.
- Osterman, G. B., R. A. Heelis, and G. J. Bailey (1994), Modeling the formation of intermediate layers at Arecibo latitudes, *J. Geophys. Res.*, *99*(A6), 11,357–11,365, doi:10.1029/94JA00519.
- Oyama, S., J. Kurihara, B. J. Watkins, T. T. Tsuda, and T. Takahashi (2012), Temporal variations of the ion-neutral collision frequency from EISCAT observations in the polar lower ionosphere during periods of geomagnetic disturbances, *J. Geophys. Res.*, *117*, A05308, doi:10.1029/2011JA017159.
- Picone, J. M., A. E. Hedin, D. P. Drob, and A. C. Aikin (2002), NRLMISE-00 empirical model of the atmosphere: Statistical comparisons and scientific issues, *J. Geophys. Res.*, *107*(A12), 1468, doi:10.1029/2002JA009430.
- Plane, J. M. C. (2003), Atmospheric chemistry of meteoric metals, *Chem. Rev.*, *103*(12), 4963–4984.
- Plane, J. M. C. (2012), Cosmic dust in the Earth's atmosphere, *Chem. Soc. Rev.*, *41*, 6507–6518, doi:10.1039/C2CS35132C.
- Plane, J. M. C., R. M. Cox, and R. J. Rollason (1999), Metallic layers in the mesopause and lower thermosphere region, *Adv. Space Res.*, *24*(11), 1559–1570.
- Plane, J. M. C., D. E. Self, T. Vondrak, and K. R. I. Woodcock (2003), Laboratory studies and modeling of mesospheric iron chemistry, *Adv. Space Res.*, *32*, 699–708.
- Plane, J. M. C., W. Feng, and E. C. M. Dawkins (2015), The mesosphere and metals: Chemistry and changes, *Chem. Rev.*, *115*, 4497, doi:10.1021/cr500501m.

- Popova, O. P., A. S. Strelkov, and S. N. Sidneva (2007), Sputtering of fast meteoroids' surface, *Adv. Space Res.*, *39*, 567–573, doi:10.1016/j.asr.2006.05.008.
- Richmond, A. D. (1995), Ionospheric electrodynamics, in *Handbook of Atmospheric Electrodynamics*, vol. II, edited by H. Volland, pp. 249–290, CRC Press, Boca Raton, Fla.
- Robinson, R. M., and R. R. Vondrak (1985), Characteristics and sources of ionization in the continuous aurora, *Radio Sci.*, *20*(3), 447–455, doi:10.1029/RS020i003p00447.
- Roble, R. G., and E. C. Ridley (1987), An auroral model for the NCAR thermospheric general circulation model (TGCM), *Ann. Geophys. Ser. A, Upper Atmos. Space Sci.*, *5*, 369–382.
- Roble, R. G., and E. C. Ridley (1994), A thermosphere-ionosphere-mesosphere-electrodynamics general circulation model (TIME-GCM): Equinox solar cycle minimum simulations (30–500 km), *Geophys. Res. Lett.*, *21*, 417–420, doi:10.1029/93GL03391.
- Roddy, P. A., G. D. Earle, C. M. Swenson, C. G. Carlson, and T. W. Bullett (2004), Relative concentrations of molecular and metallic ions in midlatitude intermediate and sporadic-E layers, *Geophys. Res. Lett.*, *31*, L19807, doi:10.1029/2004GL020604.
- Rollason, R. J., and J. M. C. Plane (1998), A study of the reactions of Fe^+ with O_3 , O_2 and N_2 , *J. Chem. Soc., Faraday Trans.*, *94*, 3067–3075, doi:10.1039/A805140B.
- Rollason, R. J., and J. M. C. Plane (2000), The reactions of FeO with O_3 , H_2 , H_2O , O_2 and CO_2 , *Phys. Chem. Chem. Phys.*, *2*, 2335–2343, doi:10.1039/b000877j.
- Ruohoniemi, J. M., and K. B. Baker (1998), Large-scale imaging of high-latitude convection with Super Dual Auroral Radar Network HF radar observations, *J. Geophys. Res.*, *103*(A9), 20,797–20,811, doi:10.1029/98JA01288.
- Rutherford, J. A., and D. A. Vroom (1972), Formation of iron ions by charge transfer, *J. Chem. Phys.*, *57*, 3091, doi:10.1063/1.1678724.
- Sandford, B. P. (1968), Variations of auroral emissions with time, magnetic activity and the solar cycle, *J. Atmos. Terr. Phys.*, *30*, 1921–1942.
- Self, D. E., and J. M. C. Plane (2003), A kinetic study of the reactions of iron oxides and hydroxides relevant to the chemistry of iron in the upper mesosphere, *Phys. Chem. Chem. Phys.*, *5*, 1407–1418, doi:10.1039/B21900E.
- Shah, M. B., P. McCallion, K. Okuno, and H. B. Gilbody (1993), Multiple ionization of iron by electron impact, *J. Phys. B: At., Mol. Opt. Phys.*, *26*, 2393–2401.
- Schunk, R., and A. Nagy (2009), *Ionospheres: Physics, Plasma Physics, and Chemistry*, 2nd ed., pp. 231–253, Cambridge Univ. Press, Cambridge, U. K., doi:10.1017/CBO9780511635342.
- Sinnhuber, M., H. Nieder, and N. Wieters (2012), Energetic particle precipitation and the chemistry of the mesosphere/lower thermosphere, *Surv. Geophys.*, *33*, 1281–1334, doi:10.1007/s10712-012-9201-3.
- Smith, J. A., and X. Chu (2015), High-efficiency receiver architecture for resonance-fluorescence and Doppler lidars, *Appl. Opt.*, *54*(11), 3173–3184, doi:10.1364/AO.54.003173.
- Solomon, S. C. (2001), Auroral particle transport using Monte Carlo and hybrid methods, *J. Geophys. Res.*, *106*(A1), 107–116, doi:10.1029/2000JA002011.
- Solomon, S. C., P. B. Hays, and V. J. Abreu (1988), The auroral 6300 Å emission: Observations and modeling, *J. Geophys. Res.*, *93*(A9), 9867–9882, doi:10.1029/JA093iA09p09867.
- St.-Maurice, J.-P., and D. G. Torr (1978), Nonthermal rate coefficients in the ionosphere: The reactions of O^+ with N_2 , O_2 , and NO , *J. Geophys. Res.*, *83*(A3), 969–977, doi:10.1029/JA083iA03p00969.
- Strang, G. (1968), On the construction and comparison of difference schemes, *SIAM J. Numer. Anal.*, *5*(3), 506–517, doi:10.1137/0705041.
- Torr, D. G. (1985), The photochemistry of the upper atmosphere, in *The Photochemistry of Atmosphere*, pp. 165–278, Academic Press, San Diego, Calif.
- Tsuda, T. T., X. Chu, T. Nakamura, M. K. Ejiri, T. D. Kawahara, A. S. Yukimatu, and K. Hosokawa (2015), A thermospheric Na layer event observed up to 140 km over Syowa Station (69.0°S, 39.6°E) in Antarctica, *Geophys. Res. Lett.*, *42*, 3647–3653, doi:10.1002/2015GL064101.
- U.S. Standard Atmosphere (1976), NOAA-S/T 76-1562, U.S. Government Printing Office: 1976 O-588-256, NOAA, NASA, U.S. Air Force, Washington, D. C.
- Vadas, S. L. (2007), Horizontal and vertical propagation and dissipation of gravity waves in the thermosphere from lower atmospheric and thermospheric sources, *J. Geophys. Res.*, *112*, A06305, doi:10.1029/2006JA011845.
- Vadas, S. L., and M. J. Nicolls (2009), Temporal evolution of neutral, thermospheric winds and plasma response using PFISR measurements of gravity waves, *J. Atmos. Sol. Terr. Phys.*, *71*, 740–770.
- Vejby-Christensen, L., D. Kella, H. B. Pedersen, and L. H. Andersen (1998), Dissociative recombination of NO^+ , *Phys. Rev. A.*, *57*(5), 3627–3634.
- Viehl, T. P., J. M. C. Plane, W. Feng, and J. Hoffner (2016), The photolysis of FeOH and its effect on the bottomside of the mesospheric Fe layer, *Geophys. Res. Lett.*, *43*, 1373–1381, doi:10.1002/2015GL067241.
- Vondrak, T., K. R. I. Woodcock, and J. M. C. Plane (2006), A kinetic study of the reactions of Fe^+ with N_2O , N_2 , O_2 , CO_2 and H_2O , and the ligand-switching reactions $\text{Fe}^+\text{X} + \text{Y} \rightarrow \text{Fe}^+\text{Y} + \text{X}$ ($\text{X} = \text{N}_2, \text{O}_2, \text{CO}_2$; $\text{Y} = \text{O}_2, \text{H}_2\text{O}$), *Phys. Chem. Chem. Phys.*, *8*, 503–512, doi:10.1039/B508922K.
- Vondrak, T., J. M. C. Plane, S. L. Broadley, and D. Janches (2008), A chemical model of meteoric ablation, *Atmos. Chem. Phys.*, *8*, 7015–7031.
- Wang, J., Y. Yang, X. Cheng, G. Yang, S. Song, and S. Gong (2012), Double sodium layers observation over Beijing, China, *Geophys. Res. Lett.*, *39*, L15801, doi:10.1029/2012GL052134.
- Whalen, J. A. (1983), A quantitative description of the spatial distribution and dynamics of the energy flux in the continuous aurora, *J. Geophys. Res.*, *88*(A9), 7155–7169, doi:10.1029/JA088iA09p07155.
- Whitehead, J. D. (1961), The formation of the sporadic-E layer in the temperate zones, *J. Atmos. Terr. Phys.*, *20*(1), 49–58, doi:10.1016/0021-9169(61)90097-6.
- Weimer, D. R. (2005), Improved ionospheric electrodynamic models and application to calculating Joule heating rates, *J. Geophys. Res.*, *110*, A05306, doi:10.1029/2004JA010884.
- Woodcock, K. R. S., T. Vondrak, S. R. Meech, and J. M. C. Plane (2006), A kinetic study of the reactions $\text{FeO}^+ + \text{O}$, $\text{Fe}^+\text{N}_2 + \text{O}$, $\text{Fe}^+\text{O}_2 + \text{O}$ and $\text{FeO}^+ + \text{CO}$: Implications for sporadic E layers in the upper atmosphere, *Phys. Chem. Chem. Phys.*, *8*, 1812–1821.
- Xue, X. H., X. K. Dou, J. Lei, J. S. Chen, Z. H. Ding, T. Li, Q. Gao, W. W. Tang, X. W. Cheng, and K. Wei (2013), Lower thermospheric-enhanced sodium layers observed at low latitude and possible formation: Case studied, *J. Geophys. Res. Space Physics*, *118*, 2409–2418, doi:10.1002/jgra.50200.
- Yu, Z. (2014), Lidar observations and numerical modeling studies of thermospheric metal layers and solar effects on mesospheric Fe layers, PhD dissertation, Univ. of Colorado Boulder, Boulder, Colo.
- Zalesak, S. T. (1979), Fully multidimensional flux-corrected transport algorithms for fluids, *J. Comput. Phys.*, *31*, 335–362, doi:10.1016/0021-9991(79)90051-2.